

---

# Development of a Lensless Microscopy Technique for Imaging Cellular Structures

---

Diploma Thesis  
in  
Physics  
at  
Ulm University

by  
**Martin Dierolf**

October 22, 2007

Supervisors at Ulm University:

Prof. Dr. sc. nat. ETH Zürich Othmar Marti  
(Institute of Experimental Physics)

Prof. Dr. Ute Kaiser  
(Electron Microscopy Group of Material Science)

Supervisor at the Paul Scherrer Institut, Villigen:

Prof. Dr. Franz Pfeiffer  
(Swiss Light Source & École Polytechnique Fédérale de Lausanne)

# Contents

<b>1</b>	<b>Introduction</b>	<b>4</b>
<b>2</b>	<b>Theory</b>	<b>6</b>
2.1	The Fourier transform and its properties . . . . .	6
2.1.1	Definition and properties . . . . .	6
2.1.2	Fourier-Bessel transform for functions with circular symmetry . . . . .	8
2.1.3	Discrete Fourier transform . . . . .	8
2.1.4	The sampling theorem . . . . .	9
2.2	Coherent electromagnetic radiation . . . . .	10
2.2.1	The scalar wave equation . . . . .	10
2.2.2	Scalar diffraction theory . . . . .	11
2.2.3	Refractive index for x-rays . . . . .	14
2.2.4	Coherence . . . . .	14
2.3	Phase retrieval . . . . .	17
2.3.1	The phase problem . . . . .	17
2.3.2	Sampling requirements . . . . .	18
2.3.3	Phase retrieval with iterative algorithms . . . . .	21
2.3.4	The Ptychographical Iterative Engine (PIE) . . . . .	26
<b>3</b>	<b>Simulations</b>	<b>32</b>
3.1	Influence of the overlap parameter on the convergence of PIE . . . . .	33
3.1.1	The overlap parameter . . . . .	33
3.1.2	Error metric . . . . .	34
3.1.3	Simulating diffraction data for different overlaps . . . . .	34
3.1.4	Simulation results . . . . .	35
<b>4</b>	<b>Experiments with visible laser light</b>	<b>38</b>
4.1	Experimental setup . . . . .	38
4.2	Data acquisition for diffractive imaging . . . . .	39
4.3	Processing of experimental data . . . . .	41

4.3.1	Determination of the illumination function . . . . .	41
4.3.2	PIE processing . . . . .	43
4.3.3	Pixel size in reconstructed images . . . . .	44
4.4	Reconstructions with different overlap parameters . . . . .	45
4.5	Toward routine lensless imaging applications . . . . .	48
<b>5</b>	<b>Diffractive imaging with hard x-rays</b>	<b>51</b>
5.1	Synchrotron radiation . . . . .	51
5.1.1	Radiation from a circular arc . . . . .	51
5.1.2	Insertion devices . . . . .	53
5.2	Experimental setup . . . . .	54
5.3	Investigated samples . . . . .	57
5.4	Results . . . . .	58
5.4.1	Fresnel zone plate . . . . .	59
5.4.2	PSI logo . . . . .	60
5.5	Limitations . . . . .	61
<b>6</b>	<b>Conclusions and outlook</b>	<b>64</b>
	<b>Bibliography</b>	<b>67</b>
	<b>List of Figures</b>	<b>73</b>
	<b>A MATLAB code for a basic PIE simulation</b>	<b>75</b>
	<b>Erklärung</b>	<b>78</b>
	<b>Acknowledgements</b>	<b>79</b>

# Chapter 1

## Introduction

If an object is illuminated with coherent electromagnetic radiation, either visible laser light or x-rays, a diffraction pattern is formed in the far-field that is related via a Fourier transform to the projection of the complex refractive index of the object. But as only intensities can be detected, the phases of the complex Fourier coefficients are lost. Thus a direct reconstruction of the object is not possible.

In the beginning of the 1970's, first iterative phase retrieval algorithms were proposed to solve this problem. The pioneering work of Gerchberg and Saxton [27] was further developed by Fienup [18, 19] to the widely used hybrid input-output algorithm. However, the first reconstruction from a x-ray diffraction pattern was not achieved until 1999 [47]. Since then, the research activities within the x-ray community in the field of 'lensless imaging' have strongly increased. This is due to the fact, that for hard x-rays today's microscopy methods are limited by the availability of high resolution optical elements. Even state-of-the-art nano-structuring techniques are not capable of producing optical elements that can achieve diffraction-limited resolution. An increase of the resolution beyond the nano-structuring limit using lensless imaging schemes is therefore of particular interest and would have significant applications in, e.g., biology and material science [62].

However, the imaging techniques based on the Fienup-type algorithms are limited to a small field of view or isolated objects of finite size and often suffer from physical constraints, convergence problems, or defocus ambiguities.

A new approach called Ptychographical Iterative Engine (PIE) combines ptychography [31] and the said standard phase retrieval algorithms. It overcomes convergence limitations and ambiguities of the latter by employing complementary diffraction data from overlapping illumination.

Within this thesis the principles of coherent diffraction microscopy are discussed with an particular focus on the PIE algorithm and its experimen-

tal realization. In chapter 2 the mathematical (section 2.1) and physical prerequisites (section 2.2) are reviewed. The general concepts of iterative phase retrieval are presented in 2.3 to provide the necessary basis for the description of the PIE algorithm. Studies on the optimization of an important parameter (overlap) by means of model calculations are reported in chapter 3. Chapter 4 discusses the experiments that were carried out with visible laser light. After a short introduction on synchrotron radiation, chapter 5 presents results of a realization of the technique with x-rays. It includes a discussion of the particular limitations experienced in practice.

Alongside with the conclusions in chapter 6 an outlook on future applications is given.

Parts of the results presented in this thesis have been included in the following publication:

O. Bunk, M. Dierolf, S. Kynde, I. Johnson, O. Marti, and F. Pfeiffer. Influence of the overlap parameter on the convergence of the ptychographical iterative engine. *Ultramicroscopy*, in print, doi:10.1016/j.ultramic.2007.08.003, 2007.

# Chapter 2

## Theory

### 2.1 The Fourier transform and its properties

All of the following definitions are given in one-dimensional notation. Generalization to more dimensions is straightforward. For functions in *direct* or *real space* the usual notation  $\mathbf{r} = (x, y, z)$  is used for the coordinates. For the Fourier transforms located in *Fourier* or *reciprocal space*, the Fourier space coordinates are written as  $\mathbf{q} = (q_x, q_y, q_z)$ . For one-dimensional notation the index may be omitted.

#### 2.1.1 Definition and properties

The complex Fourier transform  $\tilde{f}(q)$  of a square-integrable function  $f(x)$  in its continuous form is defined as [6]

$$\tilde{f}(q) = \mathcal{F}\{f(x)\} = \int_{-\infty}^{\infty} f(x) e^{-iqx} dx, \quad (2.1a)$$

with the corresponding inverse transform

$$f(x) = \mathcal{F}^{-1}\{\tilde{f}(q)\} = \frac{1}{2\pi} \int_{-\infty}^{\infty} \tilde{f}(q) e^{iqx} dq. \quad (2.1b)$$

Instead of a transformation between real and reciprocal space, the Fourier transform also describes the transformation between the time  $t$  and the angular frequency  $\omega$ . From the definitions in (2.1), several useful relations can be derived [9, 28]:

1. Similarity theorem:

$$\mathcal{F}\{f(ax)\} = \frac{1}{|a|} \tilde{f}\left(\frac{q}{a}\right). \quad (2.2)$$

A coordinate “stretching” in direct space causes a contraction of the corresponding Fourier space coordinates.

2. Shift theorem:

$$\mathcal{F}\{f(x \pm a)\} = e^{\pm iqa} \tilde{f}(q) . \quad (2.3)$$

A translation in direct space results in a linear *phase ramp* or *phase tilt* superimposed on the Fourier transform of the unshifted function.

3. Parseval’s theorem:

$$\int_{-\infty}^{\infty} |f(x)|^2 dx = \frac{1}{2\pi} \int_{-\infty}^{\infty} |\tilde{f}(q)|^2 dq . \quad (2.4)$$

Apart from a constant prefactor, the integral over the modulus squared in real and reciprocal space has the same value.

4. Convolution theorem:

$$\mathcal{F}\{f * g\} = \mathcal{F}\left\{\int_{-\infty}^{\infty} f(x')g(x-x')dx'\right\} = \mathcal{F}\{f\} \mathcal{F}\{g\} . \quad (2.5)$$

A convolution of two functions transforms to the product of their Fourier transforms.

5. Cross-correlation:

$$\mathcal{F}\{f \star g\} = \mathcal{F}\left\{\int_{-\infty}^{\infty} f(x')g^*(x'-x)dx'\right\} = \mathcal{F}\{f\} (\mathcal{F}\{g\})^* , \quad (2.6)$$

with the important special case of the autocorrelation

$$\mathcal{F}\{f \star f\} = |\mathcal{F}\{f\}|^2 . \quad (2.7)$$

6. Fourier transform of a real-valued function  $f(x) = f^*(x)$ :

$$\tilde{f}(q) = \tilde{f}^*(-q) , \quad (2.8)$$

which is also known as *Friedel’s law* in diffraction physics [1].

7. Fourier transform of derivatives:

$$\mathcal{F}\left\{\frac{d^n}{dx^n} f(x)\right\} = (iq)^n \tilde{f}(q) . \quad (2.9)$$

### 2.1.2 Fourier-Bessel transform for functions with circular symmetry

Optical setups often show circular symmetry with respect to the optical axis. This can be used to reduce two-dimensional problems involving Fourier transforms to one dimension by using the *Fourier-Bessel transform* which is also known as *Hankel transform of zero order* [9]:

$$\mathcal{H}_0 \{g(r)\} = 2\pi \int_0^\infty rg(r) J_0(rq) dr, \quad (2.10)$$

where  $J_0$  is the zeroth-order Bessel function of the first kind. Discrete versions of this transform utilize roots of the Bessel functions as sampling points. Details can be found in [29, 68].

### 2.1.3 Discrete Fourier transform

Analysis of experimental data with computers requires discretization of both the data sets and the mathematical operations (transforms). The one-dimensional discrete Fourier transform (DFT) maps an complex-valued vector  $\mathbf{f}$  of  $N$  elements to another vector space with the same dimension  $N$ . The  $n$ -th element of the transformed vector is given by [8]

$$\tilde{f}_n = (\mathcal{F} \{f\})_n = \frac{1}{N} \sum_{m=0}^{N-1} f_m e^{-2\pi i n m / N}, \quad 0 \leq n \leq N-1. \quad (2.11)$$

Then the corresponding inverse transform is

$$f_n = \left( \mathcal{F}^{-1} \left\{ \tilde{f} \right\} \right)_n = \sum_{m=0}^{N-1} \tilde{f}_m e^{2\pi i n m / N}, \quad 0 \leq n \leq N-1. \quad (2.12)$$

The theorems introduced in section 2.1.1 for the continuous case are also valid for the DFT, see, e.g., [6, 8, 46] for more details. One important additional property is the *periodicity of the DFT* so that for all  $n \in [0, N-1]$

$$f_{n+kN} = f_n, \quad \forall k \in \mathbb{Z}, \quad (2.13a)$$

$$\tilde{f}_{m+kN} = \tilde{f}_m, \quad \forall k \in \mathbb{Z}. \quad (2.13b)$$

In practice all discrete Fourier transforms are usually calculated using the *fast Fourier transform* (FFT) [12], which uses certain symmetries so that the computing time scales only with  $N \log(N)$  rather than  $N^2$  as for a standard DFT.

### 2.1.4 The sampling theorem

In practice it is important to determine the sampling intervals that have been used to sample a continuous function on a discrete, finite grid. The DFT relates the sampling step size  $\Delta q$  in Fourier space to the direct space step size  $\Delta x$  and the total number of sampling points  $N$  by

$$\Delta x \Delta q = \frac{2\pi}{N}. \quad (2.14)$$

The highest Fourier space component  $q_N$  contained in the Fourier transform is

$$q_N = \frac{N}{2} \Delta q = \frac{\pi}{\Delta x}. \quad (2.15)$$

When a function in direct space is sampled with too large intervals, spatial frequencies higher than  $q_N$  are wrapped in Fourier space and show up as lower frequencies due to the periodicity of the DFT (see eq. (2.13)). This phenomenon is known as *aliasing*. However, if a continuous function  $f(x)$  is bandwidth-limited, that is

$$\tilde{f}(q) = 0 \quad \text{for } |q| > q_{Nyq}, \quad (2.16)$$

and for this maximum spatial frequency  $q_{Nyq}$ ,

$$q_{Nyq} < q_N \quad (2.17)$$

is fulfilled, aliasing does not occur. This  $q_{Nyq}$  is called the *Nyquist frequency* or sometimes also *cut-off frequency*. Condition (2.17) translates with (2.15) to

$$\Delta x < \frac{2\pi}{2q_{Nyq}}. \quad (2.18)$$

As a consequence the function has to be sampled at intervals inversely proportional to twice the Nyquist-frequency (occurrence of the factor  $2\pi$  depends on the choice of the Fourier space variable). In this case, the function  $f(x)$  is completely determined by its sampled version  $f_m \equiv f(m\Delta x)$  [8]:

$$f(x) = \sum_{m=-\infty}^{\infty} f_m \frac{\sin q_{Nyq}(x - m\Delta x)}{q_{Nyq}(x - m\Delta x)} = \sum_{m=-\infty}^{\infty} f_m \operatorname{sinc} \frac{\pi}{\Delta x}(x - m\Delta x). \quad (2.19)$$

This form of the so called *sampling theorem* was first published by Shannon [61].<sup>1</sup> Shannon points out that a band-limited function cannot be perfectly limited in direct space as well, but may be kept very small outside a certain region. Then the infinite sums in equation (2.19) can be replaced by a finite summation with  $m = 0, \dots, N - 1$  running over all sampling points.

<sup>1</sup>Therefore it is often called the *Shannon sampling theorem*. As Shannon cites earlier work by Nyquist and Whittaker in his article, also the terms *Nyquist-Shannon sampling theorem* and *Whittaker-Shannon sampling theorem* are used.

## 2.2 Coherent electromagnetic radiation

### 2.2.1 The scalar wave equation

Although the derivation of the (scalar) wave equation from Maxwell's equations can be found in standard textbooks on electrodynamics [38, 55] or optics [5, 26], a quick overview is given here to point out the necessary assumptions and approximations. When matter is present, Maxwell's equations read:

$$\nabla \times \mathbf{H}(\mathbf{r}, t) = \mathbf{j}(\mathbf{r}, t) + \frac{\partial \mathbf{D}(\mathbf{r}, t)}{\partial t}, \quad (2.20a)$$

$$\nabla \times \mathbf{E}(\mathbf{r}, t) = -\frac{\partial \mathbf{B}(\mathbf{r}, t)}{\partial t}, \quad (2.20b)$$

$$\nabla \cdot \mathbf{D}(\mathbf{r}, t) = \rho(\mathbf{r}, t), \quad (2.20c)$$

$$\nabla \cdot \mathbf{H}(\mathbf{r}, t) = 0. \quad (2.20d)$$

The state established in space by the presence of electric charges can be described by an electromagnetic field represented by the electric field vector  $\mathbf{E}$  and the magnetic field vector  $\mathbf{H}$ . To account for the presence of a medium a second set of vectors is introduced: The electric current density  $\mathbf{j}$ , the electric displacement  $\mathbf{D}$  and the magnetic induction  $\mathbf{B}$ .  $\rho$  is the charge density. Together with the materials equations

$$\mathbf{B}(\mathbf{r}, t) = \mu_0 \mu \mathbf{H}(\mathbf{r}, t), \quad (2.21a)$$

$$\mathbf{D}(\mathbf{r}, t) = \epsilon_0 \epsilon \mathbf{E}(\mathbf{r}, t), \quad (2.21b)$$

a unique determination of the field vectors from a given distribution of currents and charges is possible. The constant  $\mu_0$  is the permeability of the vacuum,  $\epsilon_0$  its permittivity. The medium's permittivity is  $\epsilon = \epsilon(\mathbf{r}, \omega)$  and its permeability  $\mu = \mu(\mathbf{r}, \omega)$ , respectively. In the general case these are second order tensors. With the assumption, that the medium is *isotropic* they become scalars.

For the further discussion, electrically neutral, nonconducting media are assumed, i.e.,  $\rho = 0$ ,  $\mathbf{j} = 0$ , so Maxwell's equations (2.20) reduce to the homogeneous case. Then the Fourier transform with respect to  $t$  is applied on these equations and eliminates the time dependence, a common method for solving partial differential equations of this type. The argument  $(\mathbf{r}, \omega)$  is omitted in what follows.

Combining (2.21b) with (2.20c) yields

$$\nabla \cdot \tilde{\mathbf{D}} = \epsilon_0 \nabla \cdot \epsilon \tilde{\mathbf{E}} = \epsilon_0 \left( \tilde{\mathbf{E}} \cdot (\nabla \epsilon) + \epsilon \nabla \cdot \tilde{\mathbf{E}} \right), \quad (2.22)$$

which shows the necessity of another approximation: The wave equation can only be obtained if

$$\left| \tilde{\mathbf{E}} \cdot \nabla \epsilon \right| \ll \left| \epsilon \nabla \cdot \tilde{\mathbf{E}} \right|, \quad (2.23)$$

that is the variation of the electric susceptibility  $\epsilon$  can be neglected on the length scale of the variation of the electric field. The same should be true for the magnetic susceptibility  $\mu$ , which can be seen from an analogous argumentation when combining equations (2.20d) and (2.21a).

For the wave equation, we first substitute  $\mathbf{B}$  from the material equation (2.21a) into the second Maxwell equation (2.20b) and take the curl of the resulting equation:

$$\nabla \times (\nabla \times \mathbf{E}) = -\mu_0 \mu \nabla \times \frac{\partial}{\partial t} \mathbf{H}. \quad (2.24)$$

After the Fourier transform the temporal derivative is evaluated with relation (2.9), and yields

$$\nabla \times (\nabla \times \tilde{\mathbf{E}}) = -\mu_0 \mu i\omega \nabla \times \tilde{\mathbf{H}}. \quad (2.25)$$

In the first Maxwell equation (2.20a), the temporal derivative is evaluated in the same way and used to substitute  $\nabla \times \tilde{\mathbf{H}}$ , resulting in

$$\nabla \times (\nabla \times \tilde{\mathbf{E}}) = \epsilon_0 \epsilon \mu_0 \mu \omega^2 \tilde{\mathbf{E}}. \quad (2.26)$$

With the relation  $\nabla \times (\nabla \times \tilde{\mathbf{E}}) = \nabla(\nabla \cdot \tilde{\mathbf{E}}) - \nabla^2 \tilde{\mathbf{E}}$ , and  $c = 1/\sqrt{\epsilon_0 \mu_0}$  for the speed of light in vacuum and considering (2.23), we finally get

$$\nabla^2 \tilde{\mathbf{E}} + \frac{\epsilon \mu}{c^2} \omega^2 \tilde{\mathbf{E}} = 0. \quad (2.27)$$

For the magnetic field an analogous expression can be derived. Since in (2.27) the Cartesian components are decoupled and since polarization is not taken into account, it is sufficient to work only with the scalar *Helmholtz equation*

$$\nabla^2 \tilde{U}(\mathbf{r}, \omega) + k^2 n^2(\mathbf{r}, \omega) \tilde{U}(\mathbf{r}, \omega) = 0, \quad (2.28)$$

with the refractive index  $n^2 \equiv \mu \epsilon$  and the wavenumber  $k \equiv \omega/c = 2\pi/\lambda$ .

## 2.2.2 Scalar diffraction theory

For the following discussion we now assume a monochromatic scalar wave  $U(\mathbf{r}, \omega) e^{-i\omega t}$  that only has one non-zero Fourier component. We can then rewrite equation (2.28) in the form

$$\nabla^2 U(\mathbf{r}, \omega) + k^2(\mathbf{r}, \omega) U(\mathbf{r}, \omega) = -4\pi F(\mathbf{r}, \omega) U(\mathbf{r}, \omega), \quad (2.29)$$

introducing the *scattering potential* of the medium

$$F(\mathbf{r}, \omega) = \frac{1}{4\pi} k^2 (n^2(\mathbf{r}, \omega) - 1) . \quad (2.30)$$

The solution of this inhomogeneous partial differential equation can be found in the framework of potential theory by using the Green's function of the Helmholtz operator

$$G(\mathbf{r} - \mathbf{r}', \omega) = \frac{e^{ik|\mathbf{r}-\mathbf{r}'|}}{|\mathbf{r} - \mathbf{r}'|} , \quad (2.31)$$

which solves the equation

$$(\nabla^2 + k^2)G(\mathbf{r} - \mathbf{r}', \omega) = -4\pi\delta^{(3)}(\mathbf{r} - \mathbf{r}') , \quad (2.32)$$

where  $\delta^{(3)}(\mathbf{r} - \mathbf{r}')$  is the three-dimensional Dirac delta function. The physical interpretation of equation (2.31) is that a point scatterer is the source of a spherical wave. This is called the *Huygens-Fresnel principle* [5].

In principle, the field at any point can now be calculated as a superposition of the spherical wavelets from all points of a scattering object. A mathematical treatment involving Green's integral theorem leads to the *Fresnel-Kirchhoff diffraction integral*, which has an additional direction dependent factor that can not be derived from the mere Huygens-Fresnel principle. Based on such a description, the diffracted complex field  $E(X, Y)$  formed by a complex wave field  $\psi(x, y)$  (see section 2.2.3) is given by [40]

$$E(X, Y, Z) = \frac{1}{i\lambda} \iint \psi(x, y) \frac{e^{ikr}}{r} \cos(\hat{\mathbf{n}}, \hat{\mathbf{r}}) dx dy , \quad (2.33)$$

where  $(x, y)$  are object plane coordinates and  $(X, Y)$  the corresponding diffraction plane coordinates. The distance  $r$  from a point in the object plane to a point on the screen is given by  $r = \sqrt{(x - X)^2 + (y - Y)^2 + Z^2}$ , where  $Z$  is the distance from the screen to the object plane. Let  $R$  be the distance from the origin of the object system to a point  $(X, Y, Z)$ .  $\cos(\hat{\mathbf{n}}, \hat{\mathbf{r}})$  is the said directional factor where  $\hat{\mathbf{n}}$  is the unit vector of the object plane and  $\hat{\mathbf{r}}$  the unit vector along the connection of  $(x, y)$  and  $(X, Y)$ .

In the paraxial approximation, that is  $R, r \gg x, y, X, Y$ , we can set  $\cos(\hat{\mathbf{n}}, \hat{\mathbf{r}}) = 1$ , since all light travels almost parallel to the  $Z$  axis. Therefore we can set  $1/r = 1/R \approx 1/Z$ . By expanding  $r$  in the exponent around  $R$  we get

$$\begin{aligned} r &= \sqrt{(x - X)^2 + (y - Y)^2 + Z^2} \approx R \sqrt{1 - \frac{2xX + 2yY}{R^2} + \frac{x^2 + y^2}{R^2}} \\ &\approx R \left( 1 - \frac{xX + yY}{R^2} + \frac{x^2 + y^2}{2R^2} + \dots \right) . \end{aligned}$$

With these approximations, the *Fresnel approximation* of the diffraction integral is obtained:

$$E(X, Y, Z) = \frac{e^{ikR}}{i\lambda Z} \iint \psi(x, y) e^{-ik(xX+yY)/R} e^{-ik(x^2+y^2)/(2R)} dx dy. \quad (2.34)$$

For large distances from the object to the diffraction plane and for a finite size of the diffracting object, the quadratic phase factor can be neglected. The mathematical condition for this is

$$k \frac{x^2 + y^2}{2R} \ll \pi, \quad (2.35)$$

which can be rewritten for an object of size  $a$  ( $a \sim \max(x, y)$ ) and yields the so-called 'far-field condition'

$$R \approx Z \gg \frac{a^2}{\lambda}. \quad (2.36)$$

Defining the dimensionless *Fresnel number*  $f_n$ , we obtain as far-field condition

$$f_n \equiv \frac{a^2}{\lambda Z} \ll 1. \quad (2.37)$$

The electric field on the screen can then be expressed in the *Fraunhofer approximation*

$$E(X, Y, Z) = \frac{e^{ikR}}{i\lambda Z} \iint \psi(x, y) e^{-ik(xX+yY)/R} dx dy. \quad (2.38)$$

This integral is proportional to the two-dimensional Fourier transform of the complex exit wave  $\psi(x, y)$

$$E(X, Y, Z) \propto \mathcal{F}\{\psi\}(K_X, K_Y) \quad (2.39)$$

with  $(K_X, K_Y) = (kX/R, kY/R)$ .

Using the Fourier representation (2.39) in (2.34), we can calculate the wave field  $\psi_z = \psi(x, y, z)$  at distance  $z$  behind the object by multiplication with the Fresnel propagator in Fourier space:

$$\psi_z = \mathcal{F}^{-1} \left\{ e^{-\frac{izq^2}{2k}} \mathcal{F}\{\psi\} \right\}. \quad (2.40)$$

### 2.2.3 Refractive index for x-rays

For x-rays the refractive index is usually defined as

$$n = 1 - \delta + i\beta, \quad (2.41)$$

with

$$\beta = \frac{\mu\lambda}{4\pi} \quad (2.42)$$

and

$$\delta = \frac{1}{2\pi} r_e \rho_e \lambda^2. \quad (2.43)$$

Here  $\mu$  is the photoelectric absorption coefficient,  $r_e = 2.818 \cdot 10^{-15}$  m is the classical radius of the electron and  $\rho_e$  the electron density of the material. As the real part of the refractive index in equation 2.41 is smaller than 1, the phase velocity is greater than  $c$ , the speed of light in vacuum. Note that the group velocity, which represents the speed of signal transport, is smaller than  $c$ , so special relativity is not violated [1].

In case of negligible absorption, the complex exit wave can be represented by a phase factor [66]

$$\psi(x, y) = e^{i\phi(x, y)}, \quad (2.44)$$

where  $\phi(x, y)$  is equal to the optical path length difference over the sample thickness  $d(x, y)$  projected onto the  $(x, y)$  plane times the wavenumber  $k$ :

$$\phi(x, y) = \frac{2\pi}{\lambda} \int_0^{d(x, y)} \delta(x, y) dz. \quad (2.45)$$

Absorption can be taken into account by replacing  $\delta(x, y)$  by  $\delta(x, y) + i\beta(x, y)$  in the integrand. If the phase factor  $\phi(x, y)$  is real and small, we have a *weak phase object* and can expand the exponent in equation 2.44:

$$e^{i\phi(x, y)} \cong 1 + i\phi(x, y). \quad (2.46)$$

### 2.2.4 Coherence

If we consider a field formed by, e.g., the superposition of two monochromatic harmonic waves with scalar amplitude vectors  $E_{0,1}$  and  $E_{0,2}$  with different phase factors  $\varphi_1$  and  $\varphi_2$

$$\mathbf{E}(\mathbf{r}, t) = \mathbf{E}_1(\mathbf{r}, t) + \mathbf{E}_2(\mathbf{r}, t) = (\mathbf{E}_{0,1} e^{i\varphi_1} + \mathbf{E}_{0,2} e^{i\varphi_2}) e^{i(\mathbf{k} \cdot \mathbf{r} - \omega t)}, \quad (2.47)$$

the intensity pattern is given by

$$I \propto \langle |\mathbf{E}|^2 \rangle = |\mathbf{E}_{0,1}|^2 + |\mathbf{E}_{0,2}|^2 + 2\mathbf{E}_{0,1} \cdot \mathbf{E}_{0,2} \cos(\varphi_1 - \varphi_2). \quad (2.48)$$

If polarization is assumed to be the same for both waves, the existence of the interference term depends only on the phase difference  $\varphi_1 - \varphi_2$ . For a random variation of this difference the cosine term would vanish in average and there would be no interference. If a fixed relation for their phases exist, the waves are said to be *coherent*.

The general description of coherence (for more details, see, e.g., [43]) is based on evaluating the correlation of two wave fields separated in both space and time, defining it as the so-called *mutual coherence function*. Averaged over a time interval  $T$  larger than the typical fluctuations of the fields' sources one speaks of the *mutual intensity function* [52]

$$J(\mathbf{r}_1, \mathbf{r}_2) = \langle \mathbf{E}^*(\mathbf{r}_1, t) \mathbf{E}(\mathbf{r}_2, t) \rangle_T \quad (2.49)$$

where  $\mathbf{r}_1$  and  $\mathbf{r}_2$  are coordinates in a plane perpendicular to the beam and the  $E(\mathbf{r}_i, t)$  are the field values. Normalization leads to the *complex coherence factor*

$$\gamma(\mathbf{r}_1, \mathbf{r}_2) = \frac{J(\mathbf{r}_1, \mathbf{r}_2)}{\sqrt{J(\mathbf{r}_1, \mathbf{r}_1)J(\mathbf{r}_2, \mathbf{r}_2)}}. \quad (2.50)$$

The modulus  $|\gamma|$  gives the ratio of coherent intensity  $I_{coh}$  to total intensity  $I_{tot}$ . We have  $|\gamma| = 1$  for full coherence and  $|\gamma| = 0$  for total incoherence, respectively. Thus partial coherence decreases the contrast of the interference fringes. In the following the effects of partial coherence will not be discussed in further detail. Instead a simple geometrical argumentation is used to get sufficiently good estimates of the characteristic length scales, the so-called *coherence lengths*. We distinguish between temporal coherence at one point, which leads to a *longitudinal coherence length*, and spatial coherence between two points, resulting in a *transverse coherence length*.

### Transverse coherence length

To obtain an expression for the transverse coherence length of an extended source in a plane perpendicular to the optical axis, we consider Young's double-slit experiment with a one-dimensional source of height  $a$  (see figure 2.1). Small slits of separation  $d$  are placed at a distance  $R$  from the source. A screen at a distance  $L$  behind the slits is used to visualize the diffraction patterns. We now define the transverse coherence length  $\xi_t$  to be equal to the slit separation, for which the minima of the diffraction pattern from a element at the edge of the source coincide with the maxima of a diffraction pattern from a central element. The angles of the extrema in the diffraction pattern produced by such a central element are in small-angle approximation given by  $\alpha = n\lambda/d$  for the maxima and  $\alpha = (n + \frac{1}{2})\lambda/d$  for the minima with

$n \in \mathbb{Z}$ . For an element at the edge of the source, the extrema are shifted by an angle  $a/2R$ . Maxima and minima of these two patterns coincide if the condition  $\frac{1}{2} \frac{\lambda}{d} = \frac{a}{2R}$  is fulfilled and yield the transverse coherence length

$$\xi_t = \frac{\lambda R}{a}. \quad (2.51)$$

This result can be generalized to a two-dimensional source by introducing a horizontal transverse coherence length  $\xi_h$  and a vertical transverse coherence length  $\xi_v$ , respectively. For the more realistic case of a Gaussian intensity distribution in the source plane, one gets

$$\xi_h = \frac{\lambda R}{2\pi\sigma_h} \quad \xi_v = \frac{\lambda R}{2\pi\sigma_v}, \quad (2.52)$$

where  $\sigma_h$  and  $\sigma_v$  are the sigma widths of the Gaussian source intensity distribution [66].<sup>2</sup>

Especially for x-rays the transverse coherence lengths are a severely limiting factor for the size of samples in coherent diffraction experiments. For 1 Å wavelength and  $R = 40$  m distance from the source, typical coherence lengths are  $\xi_v \approx 50 - 100 \mu\text{m}$  and  $\xi_h \approx 3 - 10 \mu\text{m}$  [66].

### Longitudinal coherence length

We consider two waves with wavelengths  $\lambda$  and  $\lambda + \Delta\lambda$  starting at the same point in time and space. We define the distance at which the waves are in antiphase as the *longitudinal coherence length*  $\xi_l$  [66] as illustrated in figure 2.2. If  $\xi_l$  corresponds to  $N$  oscillations of the first wave, i.e.  $\xi_l = N\lambda$ , the second wave must have made  $N - \frac{1}{2}$  oscillations. The obtained condition  $N\lambda = (N - \frac{1}{2})(\lambda + \Delta\lambda)$  can be solved for  $N$  and then  $\xi_l = N\lambda$  yields

$$\xi_l \approx \frac{1}{2} \frac{\lambda^2}{\Delta\lambda}. \quad (2.53)$$

To observe interference, the path length difference of waves has to be smaller than the longitudinal coherence length. For a object of size  $a$ , this gives us a condition for the maximum observable diffraction angle and therefore determines the possible resolution of a reconstruction. With equation (2.14) we then obtain for the smallest samples  $\Delta x$  in real space the condition [66]

$$\Delta x \geq a \frac{\Delta\lambda}{\lambda}. \quad (2.54)$$

---

<sup>2</sup>The result can also be obtained from the complex coherence factor introduced in equation (2.50) because a Gaussian source results in a Gaussian modulus of the complex coherence factor (propagation using the Fourier transform). This allows to define the transverse coherence lengths to be equal to the sigma values of that Gaussian [52].

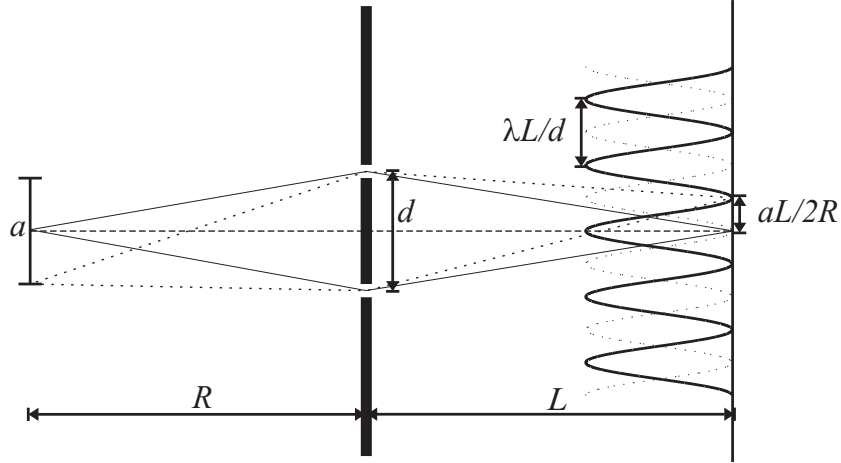


**Figure 2.1:** A Young's double-slit arrangement showing the interference patterns from two narrow slits (separation  $d$ ) illuminated from elements at the central part (solid line) and the edge (dotted line) of the source (size  $a$ ). The slit distance for which the patterns are in antiphase corresponds to the transverse coherence length  $\xi_t = \lambda R/a$ .

For a Si(111) crystal monochromator, the spectral bandwidth  $\Delta\lambda/\lambda$  is about  $1.4 \cdot 10^{-4}$  [1, p.185]. If the size of the object is  $a = 10 \mu\text{m}$  (to match transverse coherence lengths), one gets the condition  $\Delta x \geq 1.4 \text{ nm}$ .

## 2.3 Phase retrieval

### 2.3.1 The phase problem

The intensity of an electromagnetic field described by the complex scalar amplitudes  $E_0$  and  $H_0$  is given by the magnitude of its time averaged Poynting vector

$$I = \langle |\mathbf{S}| \rangle = \frac{1}{2} E_0 H_0^* = \frac{n}{2} \sqrt{\frac{\epsilon_0}{\mu_0}} |E_0|^2, \quad (2.55)$$

where  $n$  is the refractive index of the medium. Since only intensities are measured in a detector (by counting single photons or integrating the flux density), the phases of the waves are lost and have to be reconstructed. This is referred to as the *phase problem*. The importance of the phases for the reconstruction of an image from a diffraction pattern is illustrated in figure 2.3.

Given the fact that with the phases mathematically half of the information originally contained in the diffraction pattern is lost, additional constraints will be needed to make a unique reconstruction possible. For the

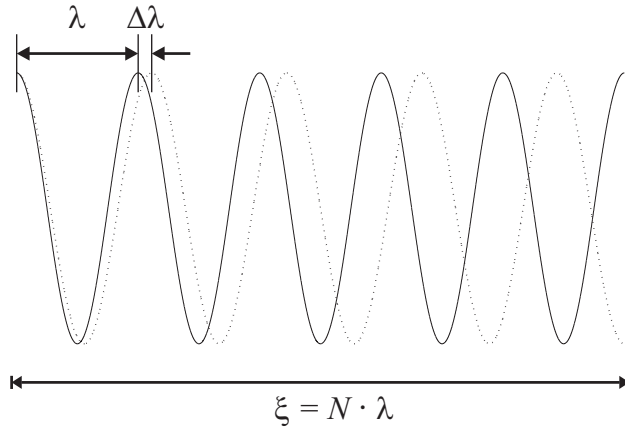


**Figure 2.2:** Two waves of wavelengths  $\lambda$  and  $\lambda + \Delta\lambda$  starting simultaneously at the same point in time and space. At the longitudinal coherence length  $\xi_l$  the phase difference has become  $\pi$ .

reconstruction itself, the actual phases are of minor interest. Thus our problem can be defined as to find the unique reconstruction which reproduces the measured diffraction amplitudes and satisfies additional constraints. The term ‘unique’ is used despite the fact that certain ambiguities are inherent to the problem, namely constant phase factors, shifts of the origin (causing phase gradients in Fourier space, see eq. (2.3)) and the so-called ‘twin image’ (complex conjugation and rotation by  $180^\circ$ ). As these are irresolvable without additional constraints, they are in the literature usually treated as equivalent solutions [2]. Breaking certain symmetries can solve the twin image ambiguity, see section 2.3.4.

### 2.3.2 Sampling requirements

Already in 1952, Sayre [60] published some implications regarding Shannon’s sampling theorem (see [61] and also section 2.1.4) and pointed out that a sufficiently fine sampling of the diffraction intensities might allow for solving the phase problem. From Shannon’s sampling theorem it can be derived, that for a function which is non-zero only on a finite interval of size  $a$  (i.e.,  $a$  is here a direct space analog to twice the Nyquist frequency), its Fourier transform has to be sampled at intervals  $1/a$  to be completely determined. This is also the typical length scale of modulations in the resulting coherent diffraction pattern. However, this sampling according to Shannon is not sufficient for phase retrieval as shall now be further discussed for two-dimensional diffractive imaging applications.

For simplicity, let us assume that the two-dimensional diffraction patterns

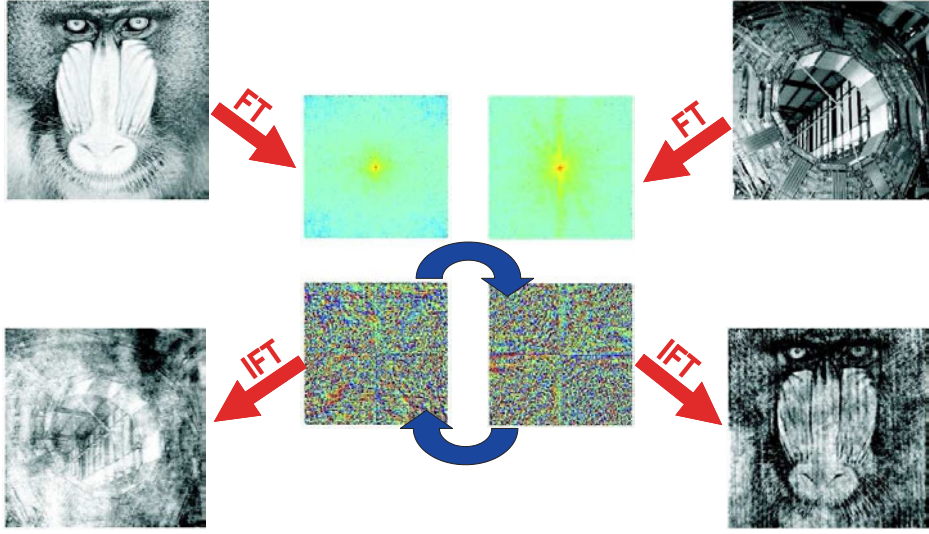


**Figure 2.3:** Illustration of the importance of Fourier phases for image reconstruction. The middle rows show the Fourier transforms of the two grayscale images, the upper the amplitude (logarithmic scale), the lower the phase. The bottom row shows the result of inverse transforms after the Fourier phases have been exchanged.

are recorded with pixelated detectors. Given a detector with  $N = N_x \cdot N_y$  pixels, the sampling intervals  $\Delta q_x$  and  $\Delta q_y$  are fixed by the detection geometry and determine the linear extent of the field of view in direct space along each Cartesian axis:

$$L_x = \frac{2\pi}{\Delta q_x}, \quad L_y = \frac{2\pi}{\Delta q_y}. \quad (2.56)$$

As the number of grid points is the same for the direct space image, (2.56) is obtained from equation (2.14) with the relations  $L_x = N_x \Delta x$  and  $L_y = N_y \Delta y$ ,  $\Delta x$  and  $\Delta y$  being the spatial sampling intervals.

We now look at an object in direct space characterized by a density function  $f(x, y)$  with a finite support  $S$ , that is

$$f(x, y) = 0, \quad \text{if } (x, y) \notin S. \quad (2.57)$$

If the maximum size of the support along each axis is given by  $S_x$  and  $S_y$ , the conditions for sufficient sampling of the object's Fourier transform are

$$\Delta q_x \leq \frac{2\pi}{S_x}, \quad \Delta q_y \leq \frac{2\pi}{S_y}. \quad (2.58)$$

This already leads to the conclusions, that for a given size of the detector samples, the object creating a diffraction pattern must not exceed a certain

size to make a reconstruction possible. As pointed out in section 2.3.1, the recorded diffraction pattern is an intensity pattern, which is proportional to the square of the object's Fourier transform. According to equation (2.7), the object's autocorrelation is obtained by a simple inverse Fourier transform of this intensity pattern. The smallest rectangle containing this autocorrelation's support has the size  $2S_x \times 2S_y$  and we get the new sampling conditions

$$\Delta q_x \leq \frac{\pi}{S_x}, \quad \Delta q_y \leq \frac{\pi}{S_y}. \quad (2.59)$$

With the sampling intervals satisfying these conditions, the intensity is sampled in a way that no aliasing in the autocorrelation occurs. As the sampling frequency is two times higher than in usual Shannon sampling, the diffraction pattern is said to be linearly *oversampled* by a factor of two, resulting in an oversampling factor of four when looking at the total number of sampling points. For the two-dimensional case (and higher dimensions), this 'almost always' [2] guarantees that the phase problem is uniquely solvable.

Miao and coworkers [49] pointed out, that unique solutions are possible with lower oversampling factors. We now consider a square image with an even number of pixels  $N$ . Components of the position vectors are given by  $q_{n,m} = (n\Delta q_x, m\Delta q_y)$  for reciprocal space and  $r_{n,m} = (n\Delta x, m\Delta y)$  for direct space, respectively. The diffraction amplitude (square-root of the actually measured intensity value) at each position  $q_{n,m}$  is then related to the object by a discrete Fourier transform (normalization constants set to 1):

$$\left| \tilde{f}(q_{n,m}) \right| = \left| \sum_{\nu,\mu=0}^{N/2-1} f(r_{\nu,\mu}) e^{i2\pi\nu\mu/N} \right|. \quad (2.60)$$

This provides us with a total set of  $N$  equations to reconstruct the  $N$  pixels of  $f(\mathbf{r})$ . But if  $f(\mathbf{r})$  is real valued, Friedel's law (see equation (2.8)) states that  $|\tilde{f}(\mathbf{q})| = |\tilde{f}^*(-\mathbf{q})|$ , i.e., the Fourier magnitude has only  $N/2$  independent values. Friedel's law breaks down for complex objects giving us  $N$  independent equations, but then we also have to reconstruct  $2N$  values, the real and imaginary parts for each pixel. To allow a unique solution the number of independent equations should match or exceed the number of unknowns. The strategy for this is to get to know the values of enough pixels of  $f(\mathbf{r})$  to reduce the number of unknowns sufficiently. This can be done by appropriately oversampling the diffraction pattern of an object with a finite support, because all values of  $f(\mathbf{r})$  outside the support are then by definition known to be zero. Defining the *oversampling ratio* [48, 49] as

$$\sigma = \frac{N}{N_S}, \quad (2.61)$$

where  $N_S$  is the amount of pixels in the support, we see that we will have enough independent equations to solve uniquely for the unknown values if  $\sigma \geq 2$  [49].

### 2.3.3 Phase retrieval with iterative algorithms

In the previous section 2.3.2 it was shown how a support constraint in direct space in combination with diffraction pattern oversampling, is mandatory for solving the phase problem. The support constraint gives us one possibility for an additional (direct space) constraint as mentioned in section 2.3.1. Other common constraints are, e.g., non-negativity of a real-valued object [19] or a known illumination [22, 53], which have some additional information compared to the mere support. Given a proper direct space constraint, the system of equations (2.60) is usually solved with iterative algorithms. The most frequently used algorithms can be understood in the framework of iterative projections onto constraint sets (see, e.g., [3, 13, 44]). Here some basic ideas will be outlined to provide the fundamentals for the discussion of the algorithm used for most of the work presented in this thesis, the Ptychographical Iterative Engine (PIE), in section 2.3.4.

#### Phase retrieval as an optimization problem

Mathematically, a complex image of  $N$  pixels can be treated as a vector  $\mathbf{x}$  with complex components  $x_\nu$  in an  $N$ -dimensional Euclidean vector space  $V_N$ . The Fourier transform changes the components of vectors but distances are invariant due to Parseval's theorem (2.4) (the transform is *unitary* because it preserves the norm). Constraints can be represented by sets of points which include all possible images that satisfy this particular constraint. Besides the Fourier modulus constraint given by the measured diffraction intensities, we use for the following discussion the support constraint introduced in section 2.3.2. Other constraints are, of course, possible. If the measured Fourier amplitudes are represented by the vector  $\mathbf{m}$ , the corresponding constraint set is

$$C_M = \{\mathbf{y} \in V_N \mid |\tilde{y}_\nu| = |m_\nu|, \forall \nu \in [1, N]\}. \quad (2.62)$$

The set  $C_S$  for a support constraint is given by all the vectors (images) for which the components have non-zero values for certain components  $\nu \in S$  and are zero for all others ( $\nu \notin S$ , i.e., outside the support  $S$ ). Mathematically this means that the dot products of a vector of the set with the basis vectors of the outside components vanish. We now can reformulate the phase retrieval problem as follows:

$$\text{find } \mathbf{x} \in C_S \cap C_M. \quad (2.63)$$

We see that firstly the constraint sets have to overlap and that secondly the intersection should ideally consist of one single point (image).

## Projections

As a projection onto a given constraint set  $D \subset V_N$ , we define the operator  $P(\mathbf{x})$  which maps every  $\mathbf{x} \in V_N$  to  $P(\mathbf{x}) = \mathbf{y} \in D$  so that the distance  $\|\mathbf{x} - \mathbf{y}\|$  is minimized, i.e.,  $\mathbf{y}$  is the closest point (image) to  $\mathbf{x}$  that satisfies the given constraint. Projectors are idempotent mappings, that is  $P(P(\mathbf{x})) = P(\mathbf{x})$ . The projection  $P_S$  for the support constraint is

$$P_S(x_\nu) = \begin{cases} x_\nu & \text{if } \nu \in S, \\ 0 & \text{otherwise.} \end{cases} \quad (2.64)$$

The Fourier modulus projection  $P_M$  is usually done in Fourier space, i.e. the projection is replaced by

$$P_M = \mathcal{F}^{-1} \tilde{P}_M \mathcal{F}, \quad (2.65)$$

with the projection in Fourier space defined as

$$\tilde{P}_M(\tilde{x}_\nu) = \begin{cases} m_\nu \frac{\tilde{x}_\nu}{|\tilde{x}_\nu|} & \text{if } \tilde{x}_\nu \neq 0, \\ m_\nu e^{i\alpha} & \text{otherwise.} \end{cases} \quad (2.66)$$

Thus in the standard case for a non-zero component  $\tilde{x}_\nu = |\tilde{x}_\nu| e^{i\phi_n}$  the amplitude in Fourier space is replaced while the phase is kept. However, for zero-valued pixels this projection is multivalued because no phase is defined and any phase  $\alpha$  will work. In practice often  $\alpha = 0$  is selected.

## Iterative projection algorithms

All common phase retrieval algorithms are based on applying these (or similar) projections onto constraint sets according to a certain scheme. If the current guess of an image is given after  $n$  iterations by  $\mathbf{x}_n$ , then we obtain the next iterate by applying a function  $G_{P_S, P_M}$  of the projectors to the current guess:

$$\mathbf{x}_{n+1} = G_{P_S, P_M}(\mathbf{x}_n). \quad (2.67)$$

The common algorithms mostly differ in the choice of  $G_{P_S, P_M}$ , overviews are given in [3] and [44]. If the iterates do not change any more, a fix-point of  $f$  with  $\mathbf{x}' = G_{P_S, P_M}(\mathbf{x}')$  has been reached, and the algorithm has converged.

- **Gerchberg-Saxton algorithm:**

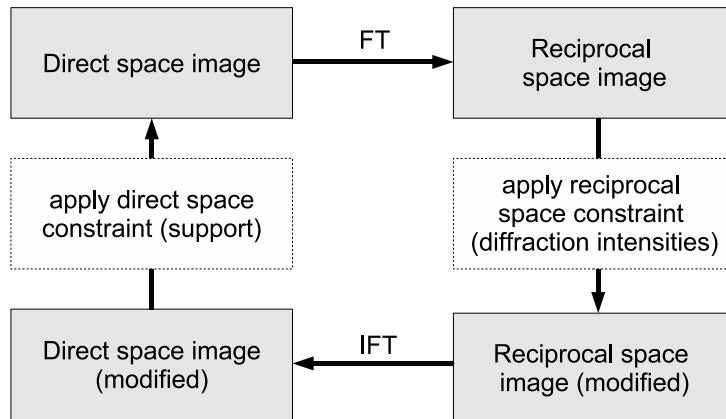


**Figure 2.4:** Schematic representation of the Gerchberg-Saxton or error-reduction algorithm [18, 27]. One starts with an arbitrary guess and iterates between direct and reciprocal space by means of the Fourier transform (FT) and its inverse (IFT), applying after each transform the appropriate constraints.

The first phase retrieval algorithm used for diffractive imaging was the *Gerchberg-Saxton algorithm* [27]. It is mostly interesting as a precursor of later work. In this algorithm the real space constraint was a second intensity measurement, a direct image of the object (as can be easily realized in a transmission electron microscope by switching between imaging and diffraction mode).

- **Error-reduction algorithm (ER):**

Fienup generalized the algorithm of Gerchberg and Saxton by introducing the non-negativity and the support constraint and called this the *error-reduction algorithm*<sup>3</sup> [18, 19]. Of course, a direct space image may also be regarded as a special way of defining a non-negativity or support constraint, but for the further development it was important to do this generalization step. It gives, e.g., the flexibility to start only with a diffraction pattern and a guess of a relatively loose support, usually obtained by looking at the autocorrelation of the diffraction pattern [23]. This loose support is then refined during reconstruction by thresholding techniques [45, 65] to get the tight support necessary for a good reconstruction. Another suggestion is to use a too small support in the beginning and enlarge it during reconstruction [19].

For the error-reduction algorithm the updating rule (2.67) takes the

---

<sup>3</sup>Often the difference of the direct space constraints is not accounted for and the terms ‘error-reduction algorithm’ and ‘Gerchberg-Saxton algorithm’ are used as synonyms, as already Fienup did.

form

$$\mathbf{x}_{n+1} = P_S(P_M(\mathbf{x}_n)). \quad (2.68)$$

The name error-reduction is based on the behavior of these alternating projections: Each projection always finds the closest point on the other constraint set, so the distance between the two sets is continuously minimized. But this also means, that the algorithm easily gets stuck in local minima of this distance.

In practice one usually starts with an arbitrary guess for the image in direct space and calculates the next iteration according to (2.68). Taking into account that the  $P_M$  projection includes one Fourier transform and one inverse Fourier transform, the algorithm can be represented as a cycle with four steps, as schematically shown in figure 2.4. In principle, the starting point can be any of these positions. Repeating the algorithm several times with different random starting images is a common method to judge whether a reconstruction is unique.

- **Input-output algorithms and further developments:**

To avoid the stagnation problems of the error-reduction algorithm, Fienup proposed so-called ‘input-output’ algorithms [18, 19] as a further generalization. Here ‘input’ and ‘output’ refer to the images before and after applying the Fourier modulus projection. The new input is now not just obtained by applying the object domain constraint on the output. In fact the next input is constructed by using the difference between the obtained output and the input which produced it in a feedback function. The idea is to minimize this difference and no longer the difference between images satisfying the two constraints individually, as it is done in the error-reduction algorithm. The input is usually no longer an estimate of the object, so here the fixed point of the iterates is usually not directly the solution of the phase retrieval problem. For a certain choice of the update function, one gets the error-reduction algorithm as a special case of an input-output algorithm.

Still widely used is the following formulation, Fienup’s *hybrid input-output algorithm* (HIO):

$$\mathbf{x}_{n+1}(\nu) = \begin{cases} P_M(x_n(\nu)) & \text{if } \nu \in S \\ \mathbf{x}_n(\nu) - \beta P_M(\mathbf{x}_n(\nu)) & \text{if } \nu \notin S, \end{cases} \quad (2.69)$$

where  $\nu$  are the pixel indices and  $S$  is the set of all pixels that satisfy the real space constraint, e.g., lie inside a known support. The feedback parameter  $\beta$  is typically chosen to be slightly smaller than unity, which

gives the best performance of the algorithm [19]. Combining the two cases of equation (2.69) by expressing them with the projector  $P_S$  on the support constraint, one gets

$$\mathbf{x}_{n+1} = \mathbf{x}_n + (1 + \beta)P_S(P_M(\mathbf{x}_n)) - P_S(\mathbf{x}_n) + P_M(\mathbf{x}_n) \quad (2.70)$$

as an iteration rule.

The HIO algorithm is still the basis for many reconstructions done in the field of diffractive imaging. Of course, several other algorithms have been developed in the past 25 years, for a comparison of the most prominent see [44]. The most general projection-based algorithm in use is probably the *difference map* [13]. The HIO algorithm turns out to be just a special case of this more general approach. Besides its application in diffractive imaging [64, 65], the difference map can be used for general optimization problems which can be formulated in terms of two constraints, e.g., protein folding problems or Sudoku puzzles [14].

### Limitations of common algorithms

- **Requirement for isolated sample:**

For the algorithms discussed so far, the sample has to be isolated due to the required oversampling (see section 2.3.2) and – in the case of x-rays – the limited coherence of the illuminating field (see section 2.2.4). This can make sample preparation extremely challenging, because already small scattering signals from outside the support can cause significant effects (in [65], e.g., the effect of small dust particles next to the actual sample (a yeast cell) is discussed).

Alternatively the direct space constraint of an isolated scattering object can also be fulfilled by constraining the illumination appropriately (‘illumination pattern constraint’, [22]), e.g. by using a pinhole in front of the object. This would allow to move an extended object with respect to the illumination, record diffraction patterns for several positions, reconstruct each pattern separately and combine the resulting images. Considering that typically several thousand iterations are done to get a sufficiently good reconstruction from an experimental diffraction pattern [11, 62], this seems not feasible for too many positions.

- **Convergence issues:**

The mentioned high number of required iterations may also be a limiting factor for certain cases, in which fast first images are desired, e.g.,

when imaging an unknown extended sample which only has a particular region that is of interest for a high resolution analysis.

The problems of stagnation or convergence to the twin image (or the superposition of the ‘true’ solution and the twin image) are quite common for symmetrical supports: Breaking the symmetry can solve these problem [24], but may not be possible in all cases.

- **Reconstruction of complex-valued objects:**

If it comes to complex-valued objects, having both absorbing and phase-shifting properties, the strong non-negativity constraint breaks down and a extremely tight support, usually of a certain type (highly asymmetric or consisting of several unconnected parts), is required to get reasonable results [20].

- **Defocus ambiguity:**

The algorithms also show problems to settle at the right plane for reconstruction within the depth of the illumination, so defocus ambiguities are also likely in many cases [63].

- **Experimental noise:**

In the presence of noise an intersection of the constraint sets may no longer be guaranteed, causing convergence problems that require some special treatment.

Currently two main approaches are experimentally realized to overcome some of these limitations: The first is the so-called *Fresnel Coherent Diffractive Imaging* (FCDI) method [51, 53, 67], which uses a well-defined illumination with a curved wavefront to improve convergence and solve uniqueness problems. The second is the *Ptychographical Iterative Engine* (PIE) that will be discussed in detail in the next section.

### 2.3.4 The Ptychographical Iterative Engine (PIE)

#### Ptychography

Few years before the Gerchberg-Saxton algorithm was published, Hoppe proposed a direct (non-iterative) technique to retrieve phases for crystallographic specimens in transmission electron diffraction microscopy [31]. The basic idea is to use a finite coherent illumination of the size of one unit cell. In the diffraction pattern this results in a convolution of the illumination’s Fourier

transform with the crystal’s Bragg peaks. If the size of the illumination is chosen appropriately, the patterns from adjacent Bragg peaks start to overlap. The interference in the overlap region can be used to determine the relative phase. Hoppe showed that the remaining ambiguity between the correct solution and its complex conjugate can be removed by recording diffraction patterns at two slightly different positions [31]. The technique was later named *ptychography* [30], derived from the Greek word for ‘fold’,  $\pi\tau\nu\xi$ , to refer to the convolution involved. Hoppe also discussed the extension to non-periodic objects, for instance with phase-shifting plates, and to scanning transmission electron diffraction microscopy in two and three dimensions [32]. Besides some proof-of-principle studies [50], the technique has not been widely used (in 1982, Hoppe called it one of his two ‘nearly forgotten ideas’ [33]). The same is true for the related Wigner-distribution deconvolution [10, 56], an extension to non-crystalline objects.

### Ptychographical iterative phase retrieval

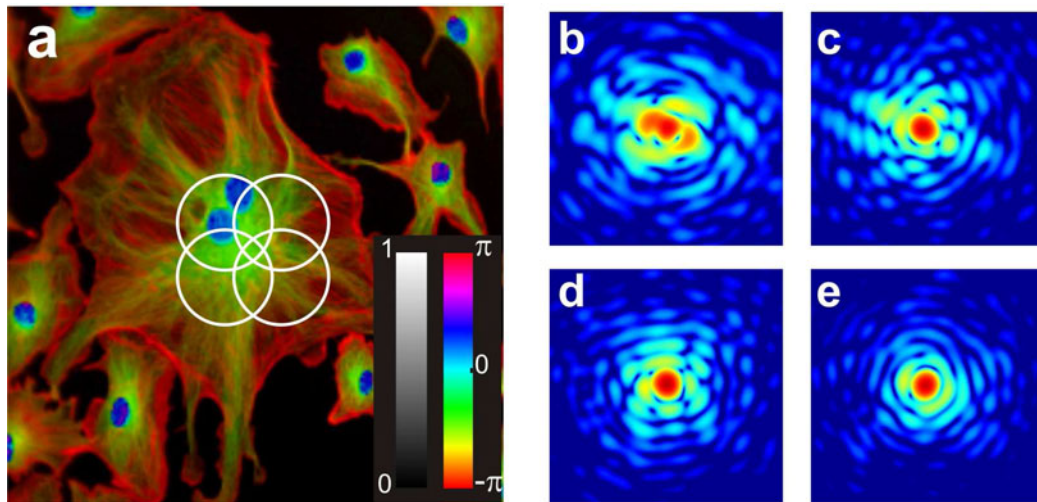


**Figure 2.5:** Simulation of PIE data collection for four overlapping probe positions. Illuminating the complex-valued object (a) with circular probes (indicated by the white circles) yields the diffraction patterns (b)–(e). The real-valued Fourier magnitudes (b)–(e) are plotted on a color-coded logarithmic scale. Image (a) codes phase and amplitude information as brightness and hue according to the colorbars.

Faulkner and Rodenburg [16, 57] suggested to combine elements of ptychography and iterative phase retrieval algorithms to a scheme they called *Ptychographical Iterative Engine* (PIE). The algorithm uses the redundant information of diffraction patterns taken with overlapping illuminations at different

positions of the probe with respect to the sample. Figure 2.5 illustrates the principle of the data collection. In practice this can be done by either scanning the illuminating probe (for example in electron microscopy) or scanning the sample with respect to the probe, as it was done in our case.

The PIE algorithm overcomes most of the limitations mentioned in section 2.3.3. The twin image problem is resolved by the broken symmetry of the problem due to the knowledge that in the overlapping region the reconstructions from neighboring probe positions must be consistent. The data from several sample positions with overlapping illuminations also leads to a solution at one well-defined defocus value (i.e., the plane of the object), solving the focal plane ambiguity. The algorithm can routinely deal with complex-valued objects and converges fast. The technique is therefore well-suited to image extended objects without any prior knowledge on the objects.

The error tolerance of the algorithm has been investigated [17] and is remarkable when it comes to experimental noise. But the algorithm turns out to be very sensitive to errors in shape or positioning of the illumination, so a good knowledge of these is mandatory.

## Description of the algorithm

The PIE algorithm can be regarded as a special type of input-output algorithm. The basic idea is not to process the diffraction patterns independently, but let the algorithm run as loop over all probe positions, at each of which an iteration similar to HIO is performed and passed further as input to overlapping positions.

For the mathematical description, we look at a complex-valued probe function  $P(\mathbf{r})$  with  $\mathbf{r} = (x, y, 0)$  (two dimensional images).  $P$  may be limited in bandwidth, with soft edges or even have an infinite extent as long as it is ‘substantially’ localized [58], so that the oversampling condition is still fulfilled. This probe is incident on the complex-valued object  $O(\mathbf{r})$ , resulting in a complex exit wave  $\Psi(\mathbf{r}) = P(\mathbf{r})O(\mathbf{r})$ . The measured diffraction intensities  $I(\mathbf{q})$  are in the far-field proportional to the squared magnitude of the exit field’s Fourier transform:  $I(\mathbf{q}) \propto |\mathcal{F}\{\Psi(\mathbf{r})\}|^2$ . The momentum transfer  $\mathbf{q} = (q_x, q_y, 0)$  is given by the difference between the wave vectors of the incident  $\mathbf{k}_0$  and the scattered waves  $\mathbf{k}_s$ , i.e.,  $\mathbf{q} = \mathbf{k}_s - \mathbf{k}_0$  with the wave numbers  $|\mathbf{k}_0| = |\mathbf{k}_s| = k = 2\pi/\lambda$  (elastic scattering). The momentum transfer  $q_z$  along the beam is considered to be negligible (flat Ewald sphere). The practical calculation can be done with Bragg’s law,

$$|\mathbf{q}| = 2k \sin(\theta), \quad (2.71)$$

using the wavelength  $\lambda$  and the angle  $2\theta$  between the incident ( $\mathbf{k}_0$ ) and the

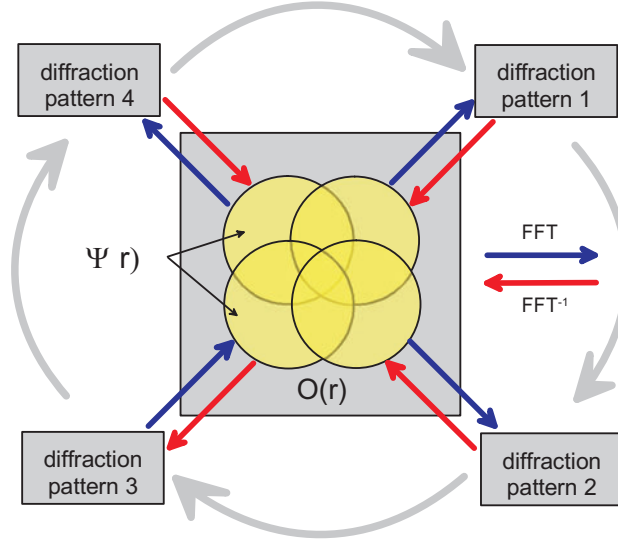


**Figure 2.6:** Schematic representation of the PIE algorithm for data taken at four different illumination positions (see figure 2.5). The outer circular arrows indicate the position stepping within one iteration. The straight arrows inside indicate (inverse) Fourier transforms. The four recorded diffraction patterns provide the usual Fourier magnitude constraint, the real space constraint is given by the circular illumination. It is multiplied with the object function  $O(\mathbf{r})$  at appropriate positions to get the exit waves  $\Psi(\mathbf{r})$  used in the reconstruction, see text for more details. From [59].

scattered ( $\mathbf{k}_s$ ) beam. The different positions of the sample with overlapping illumination are given by a vector  $\mathbf{R}_l$ , that specifies the shift of the  $l$ th sample position with respect to the arbitrarily chosen origin.

The starting point for the first iteration  $n = 1$ , is an arbitrary guess for the object function  $O(\mathbf{r})$ , for example an image with random pixel values. The updated object function, here  $O_{n+1}$  after  $n + 1$  iterations, is obtained with the following steps [7, 17] (compare figure 2.6).

1. Calculate the exit wave field from the known illumination and the current guess of the object:

$$\Psi_{n,l}(\mathbf{r}) = P(\mathbf{r})O_n(\mathbf{r} - \mathbf{R}_l). \quad (2.72)$$

2. Obtain amplitude and phase in reciprocal space using the Fourier transform:

$$\mathcal{F}\{\Psi_{n,l}(\mathbf{r})\} = A_{n,l}(\mathbf{q})e^{i\phi_{n,l}(\mathbf{q})}. \quad (2.73)$$

3. Correct the amplitude to the measured values:

$$A_{n,l,\text{new}}(\mathbf{q}) = \sqrt{I_l(\mathbf{q})}. \quad (2.74)$$

4. The inverse Fourier transform yields an updated guess of the exit field:

$$\Psi_{n,l,\text{new}}(\mathbf{r}) = \mathcal{F}^{-1} \left\{ \sqrt{I_l(\mathbf{q})} e^{i\phi_{n,l}(\mathbf{q})} \right\} = \mathcal{F}^{-1} \left\{ A_{n,l,\text{new}}(\mathbf{q}) e^{i\phi_{n,l}(\mathbf{q})} \right\}. \quad (2.75)$$

5. Update the object at the currently illuminated position:

$$O_{n+1}(\mathbf{r} - \mathbf{R}_l) = O_n(\mathbf{r} - \mathbf{R}_l) + \beta U(\mathbf{r}) (\Psi_{n,l,\text{new}}(\mathbf{r}) - \Psi_{n,l}(\mathbf{r})), \quad (2.76)$$

with the update function

$$U(\mathbf{r}) \equiv \frac{|P(\mathbf{r})|}{\max(|P(\mathbf{r})|)} \frac{P^*(\mathbf{r})}{|P(\mathbf{r})|^2 + \alpha}. \quad (2.77)$$

6. Move to the next position  $\mathbf{R}_{l+1}$ , for which the illumination partly overlaps with that of the previous position, and start the next cycle. The overlap causes that  $O_{n+1}(\mathbf{r} - \mathbf{R}_{l+1})$  in (2.72) will include also a contribution from  $O_{n+1}(\mathbf{r} - \mathbf{R}_l)$  obtained in the previous cycle from (2.76).

7. Repeat the previous steps for all sample positions  $l$  and as many iterations  $n$  as wanted. As a measure for convergence, e.g., the deviation between the measured intensities and the ones calculated in (2.73) from the current guess of the object can be used by defining a sum squared error [42]

$$S_n = \frac{\sum (I_l - A_{n,l}^2)^2}{\sum I_l^2}. \quad (2.78)$$

The summation runs over all sample positions  $l$  and all pixel intensities at each of these positions resulting in a real-valued scalar. Another common metric is based on monitoring the difference of the images obtained at two consecutive iterations [19].

When looking in more detail at the updating procedure in equation (2.76), we observe that one PIE iteration  $n \rightarrow n+1$  consists of an entire pass over all diffraction patterns, running the steps (1) to (5). In standard algorithms we have only one use of the update function per iteration. This should be kept in mind when comparing iteration numbers. The parameter  $\beta$  is closely related to the feedback parameter in Fienup's HIO and is usually chosen to be in the same range, i.e.,  $\beta \in [0.9, 1.0]$ . The parameter  $\alpha$  in the update function (2.77) prevents a division-by-zero occurring if  $P(\mathbf{r}) \sim 0$ . For a probe normalized to 1, for example a value of  $\alpha = 0.001$  may be used. The first expression in the update function  $|P(\mathbf{r})|/\max(|P(\mathbf{r})|)$ , maximizes the update effect in regions where  $|P(\mathbf{r})|$  is large. Thus strongly illuminated areas contribute

more than weakly illuminated ones, attenuating errors that otherwise might occur [17]. The second term  $P^*(\mathbf{r})/(|P(\mathbf{r})|^2 + \alpha)$  removes the multiplication with the probe function in equation (2.72) from the exit wave leaving the object function.

From the input-output point of view, the input is the new exit wave obtained by inserting the new object from (2.76) in (2.72) (which in combination would just give an update function for the exit wave). The output is the new guess of the exit wave field according to (2.75).

# Chapter 3

## Simulations

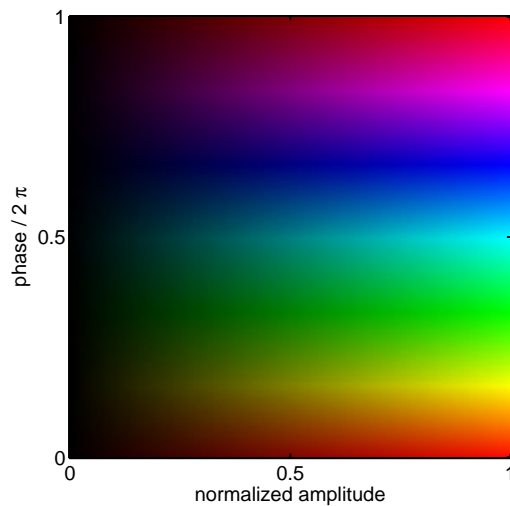


**Figure 3.1:** Hue-brightness encoding of complex images: The normalized amplitude is encoded as brightness according to the horizontal axis. The vertical phase axis may be cyclically shifted as an arbitrary overall offset remains undetermined in reconstructions.

Simulations have the advantage, that the original object is perfectly known and so the quality of the reconstruction can be directly assessed with an adequate error metric. Therefore the performance of algorithms can be easily compared and evaluated for different values of the important parameters. A sample code for a PIE reconstruction from four simulated diffraction patterns can be found in appendix [A](#).

All simulations were done with MATLAB (The Mathworks). As it has its strengths in matrix-based operations, it is perfectly suited for simulating two-dimensional imaging problems. Complex wave functions are represented as

complex matrices and are usually visualized by either separately plotting the amplitude and phase values or, as it is usually done in this thesis, by a color-coded representation: The normalized amplitude determines the brightness of the pixels, while the phase (modulo  $2\pi$ ) is coded as hue (see figure 3.1). As the reconstruction procedures are insensitive to constant global phase factors  $e^{i\gamma}$  ( $\gamma \in \mathbb{R}$ ), the phase axis may be cyclically shifted by subtracting a certain phase offset from the image.

## 3.1 Influence of the overlap parameter on the convergence of PIE

### 3.1.1 The overlap parameter

As pointed out in section 2.3.4, the advantages of the PIE technique are mainly based on the huge amount of redundant information recorded from the overlapping illuminations. The two limiting cases are full and no overlap: If the illuminations do not overlap, the reconstruction for each sample position becomes independent from the data recorded at other positions. Then the PIE algorithm (section 2.3.4) becomes a standard input-output algorithm<sup>1</sup> for each position separately. For full overlap we have a standard phase retrieval problem with only a single diffraction pattern and illumination constraint. In what follows the term ‘overlap’ will refer to linear distance overlap, not an area overlap. For two circular illumination functions of radius  $r$  and the center-to-center distance  $a \in [0, 2r]$ , the absolute linear overlap is  $o_{\text{abs}} = 2r - a$ . Normalization by the diameter of the circles gives the relative overlap

$$o = 1 - \frac{a}{2r}. \quad (3.1)$$

The advantage of the linear overlap is that usually the directly related  $a$ , the step size between adjacent positions, is the parameter needed to specify a PIE scan. The change of the probe due to free-space propagation is neglected in the calculation of the overlap, i.e., for  $r$  always the radius of the pinhole is used.

For the first successful experiment with laser light an overlap of 37.5% has been reported [58] and in a proof-of-principle study with x-rays [59], the overlap was half the diameter of the pinhole, i.e., 50%. In principle, the overlap should be as big as possible to maximize the redundancy in the data without losing the symmetry-breaking effects of the sample shifting. From

---

<sup>1</sup>The update function differs from the *hybrid* input-output (HIO) update function by the weighting with the normalized modulus of the probe.

a practical point of view this is not very useful: If one wants to scan a certain area an increase of the overlap will not only increase the number of scanning positions and thus the total acquisition time and amount of data. For radiation sensitive samples this will also result in a much higher dose and thereby degradation.

### 3.1.2 Error metric

The error metric should allow to quantify the deviations of the retrieved complex-valued object  $O_n$  after  $n$  iterations of the algorithm from the true solution  $O$ . One important prerequisite is invariance of the error metric under global phase offsets  $e^{i\gamma}$  ( $\gamma \in \mathbb{R}$ ) which may occur in both standard phase retrieval and PIE. Fienup has proposed error metrics [21], which are invariant under all of the inherent ambiguities of standard phase retrieval described in section 2.3.1. We explicitly did not use the additional terms that make the error metric invariant under replacement of the image by the its twin image: In the framework of PIE twin images are no longer an inherent ambiguity due to the symmetry-breaking properties of the technique. So our metric is defined as [21]:

$$E \equiv \left( \frac{\sum |O_n|^2 + \sum |O|^2 - 2|\sum OO_n^*|}{\sum |O|^2} \right)^{1/2}. \quad (3.2)$$

The summations are over all pixels of the images.

### 3.1.3 Simulating diffraction data for different overlaps

For the simulations the fluorescence image of a cell already shown in figure 2.5(a), page 27, was used [37]. The illumination was defined by a circular aperture of 200  $\mu\text{m}$  diameter (represented by 40 pixels) that was in a distance of  $z = 2.5$  mm from the object. The probe  $P_z$  at the distance  $z$  behind the pinhole was calculated from the modeled probe at the pinhole position  $P_0$  by multiplication with the Fresnel propagator in Fourier space:

$$P_z = \mathcal{F}^{-1} \left\{ e^{-\frac{izq^2}{2k}} \mathcal{F} \{P_0\} \right\}, \quad (3.3)$$

with  $k = 2\pi/(632.8 \text{ nm})$ . The object had  $201 \times 201$  pixels corresponding to  $5 \mu\text{m} \times 5 \mu\text{m}$  each. The detector was assumed to be in the far-field, so the diffraction plane was linked to the object plane by a discrete Fourier transform. To assess the optimum overlap, the object was illuminated with  $5 \times 5$  object positions placed on a square grid. The overlap of these illumination functions was changed in 41 steps from 0% to 100%.

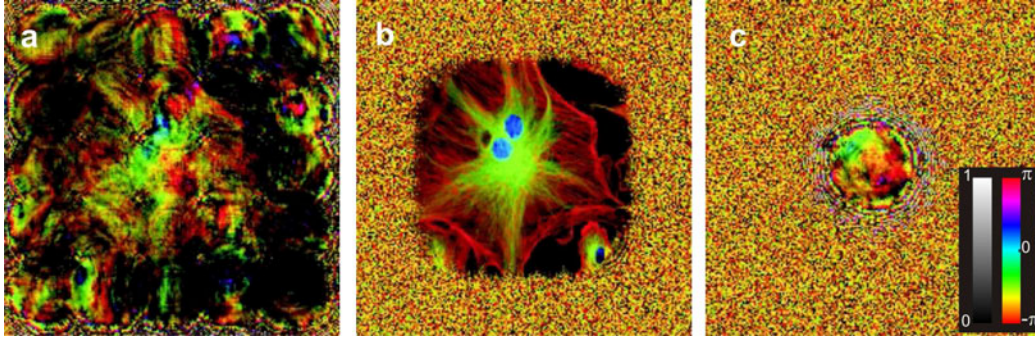


**Figure 3.2:** Reconstructions of simulated data for different relative overlaps. Each image has been retrieved in 30 PIE iterations over  $5 \times 5$  object positions. The relative illumination overlaps were 10% (a), 60% (b), and 100% (c).

### 3.1.4 Simulation results

The reconstructions were done with an implementation of the PIE algorithm as introduced in section 2.3.4. Some exemplary reconstruction results for three of the 41 different simulated overlap positions are shown in figure 3.2. In figure 3.2(a) the relative overlap is 10%. After 30 PIE iterations the similarity to the original image (see figure 2.5(a)) is hardly visible, but the overall shape of the cell can already be seen. A closer look on the phase shows, that in the single circles superpositions of the twin image and the ‘real’ image occur. When the relative overlap is increased to 60%, see figure 3.2(b), it is not possible to distinguish by eye the retrieved image from the original one. For full overlap, as shown in figure 3.2(c), PIE reduces to a conventional input-output algorithm. Taking into account, that the 30 PIE iterations over 25 totally overlapping positions correspond to 750 iterations at the central position, the quality of the retrieved image is rather poor.

To quantify the results the error metric introduced in equation (3.2) was monitored as a function of the overlap of neighboring positions. The error was calculated for the central disk of the  $5 \times 5$  illuminations to avoid edge effects and to neglect unilluminated areas. For each overlap positions, 30 PIE iterations were done with 25 different random starting guesses. The average error and its standard deviation are plotted in figure 3.3(a) as a function of the relative overlap and for different numbers of PIE iterations. Concerning the overlap, two major results are observed: (i) The best quality of the reconstructed image is achieved for a very high overlap of about 85%. Higher overlaps are inadvisable, as the gradual transition to a standard input-output algorithm in the range from about 85% to 100% results in a rapid increase of the error  $E$ . (ii) A sufficient relative overlap of at least 50% and as

little as five PIE iterations may already yield an acceptable image quality for fast overview scans. For only 30 PIE iterations the image quality is excellent, showing only minor, barely measurable improvements.

For practical purposes it is of interest, what the optimum overlap is when taking the total measurement time and the radiation dose on the sample into account. The optimum overlap will clearly not any longer be about 85%. Its value will rather depend on various factors, e.g., the weight given to acquisition time relative to image quality, whether the radiation damage starts only after a certain minimum dose or evolves continuously from the start and also the form of progression of the radiation damage. As these factors highly depend on the specific experiment, we used a simple model where we calculated the dose as the illumination hitting a pixel of the object. The incident probe  $P$  was normalized to 1, so a dose of, e.g., 2.0 referred to the corresponding pixel being fully illuminated twice. As a guide-line figure 3.3(b) shows plots of the error multiplied with the dose. If one is interested in an optimum trade-off between total scanning time and image quality and if the scanning time overhead is quantified via unnecessary over-exposures, then the same result would be obtained. The plots suggests an optimum relative overlap of less than 60%. The minimum relative overlap for complete coverage, in the case that the illumination positions are arranged on a square grid and propagation effects are neglected, is  $1 - 2^{-1/2} \approx 29\%$ . This value is consistent with the large decrease of the error seen in the plots around 30%. Although the error at such small overlap values is significantly higher than under optimal conditions, it can still be of interest if radiation damage and speed are a major concern.

The simulations were repeated with other test images and gave qualitatively the same error plots indicating some general validity. When placing the illuminations on a hexagonal grid, the minimum overlap for which the error started to decrease significantly, reduced to a value where complete-coverage in the hexagonal grid is reached. Apart from that, the principle trend remained qualitatively the same. Due to the two-dimensionality of the illumination function, it is also sufficient, if overlap is only present along one dimension. This may be of interest for certain applications where only line scans are required.

To summarize the results of the simulations: If one emphasizes the image quality without completely neglecting the dose on the sample and the time needed for the measurements, a relative overlap of 60% seems to be reasonable. If dose is not an issue, the overlap should not exceed more than about 85% for optimum performance of the algorithm. For very fast overview scans and highly radiation sensitive samples, relative overlaps of only 30% are recommendable.

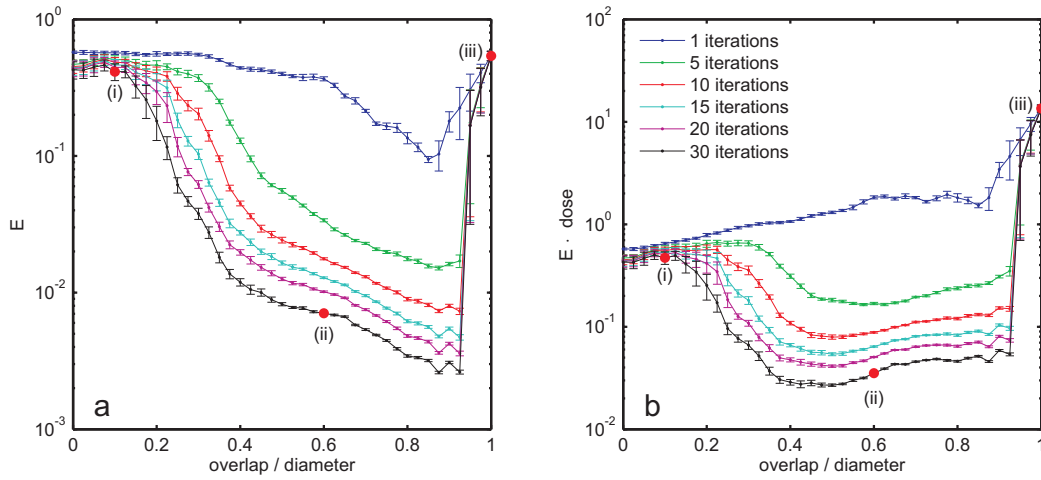


**Figure 3.3:** Error as a function of the relative overlap of the illuminated areas for different numbers of PIE iterations. In (a) the error  $E$  as a measure for the quality of the reconstructed image is plotted. In (b) the dose on the sample is linearly taken into account by plotting  $E$  times the dose. The error bars give the standard deviation when averaging the results of 25 simulation runs starting with different random guesses. The red dots mark relative overlaps of 10% (i), 60% (ii) and 100% (iii), corresponding to the reconstructions in figure 3.2.

Experimental results for different amounts of overlap are discussed in section 4.4.

# Chapter 4

## Experiments with visible laser light

### 4.1 Experimental setup

The setup is schematically depicted in figure 4.1, figure 4.2 shows photos of the practical realization. As a light source a helium-neon laser with a wavelength of  $\lambda = 632 \text{ nm}$  was used (Melles Griot 25 LHP 151-230, continuous wave, 5 mW, TEM<sub>00</sub>, random polarization). The illumination function incident on the sample was defined by a pinhole as close as geometrically possible to the sample. Typical pinhole diameters were 200  $\mu\text{m}$  or 300  $\mu\text{m}$  and the typical pinhole to sample distances were in the range of 1 – 2.5 mm. The diameter  $d$  of the exit aperture of the laser and the distance  $\rho$  from the laser to the illuminating pinhole were chosen in a way, that  $d^2/(\rho\lambda) \ll 1$ . Then the pinhole can be regarded as being illuminated with a plane wave. The sample was motorized by stepper motor driven linear translation stages (Newport MFA-PP), giving a translation range of 25 mm at a half-step size of approximately 0.24  $\mu\text{m}$  along each of the three Cartesian axis. Between sample and detector various optical elements (Edmund Optics) could be mounted for different purposes: In some experiments, the property of a convex lens to produce the Fourier transform of the incident field at its focal plane [28] was used to record far-field diffraction patterns when the geometrical far-field condition in terms of distance from the object to the detector was not fulfilled. Various neutral density filters and a narrow bandpass filter could be used to reduce the effect of stray light and to adapt the incoming intensity to the detector's sensitivity. The detector, a charge coupled device (CCD, Finger Lakes Instrumentation, IMG 1001E), was placed around 20 cm downstream from the sample. The CCD chip of 16 bit dynamic range with

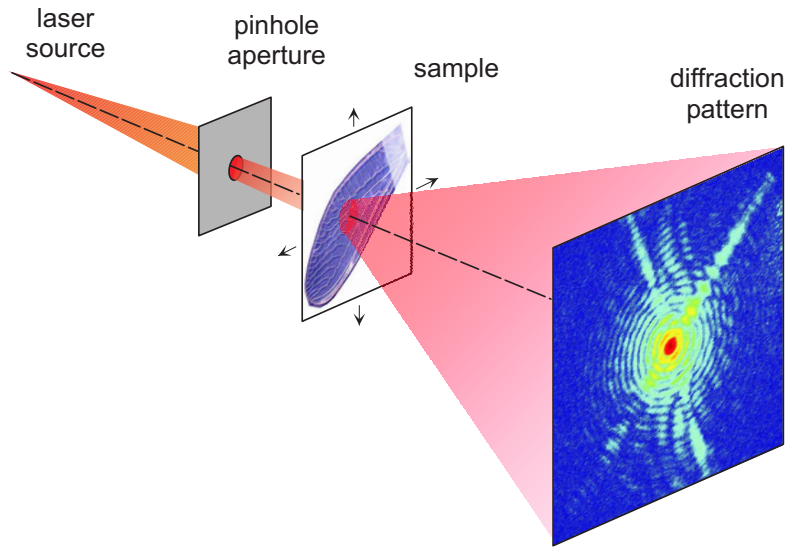


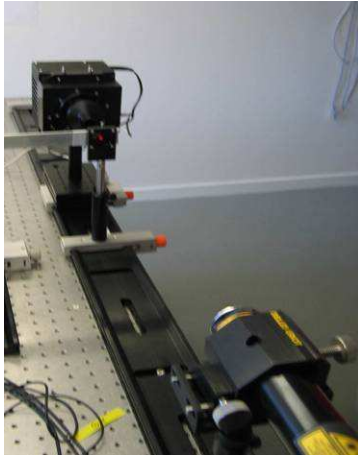
**Figure 4.1:** Laser PIE setup. The probe is defined by a pinhole illuminated with a HeNe laser. The sample can be scanned in a plane perpendicular to the propagation direction of the incident beam. The diffraction pattern is recorded with a CCD detector. From [7].

1024 × 1024 pixels of 24 μm × 24 μm was Peltier cooled to −25 °C to reduce the number of dark counts. If the filters were used they were connected to the CCD by a light-tight tube of C-mount and T-mount elements (Edmund optics). All components of the setup were placed on a rail (Linos) with holders (Ekspla) that allowed manual tilts and translations for adjustment. The rail was mounted on an optical table. The control of sample positioning and the detector were done with the software *spec* (Certified Scientific Software).

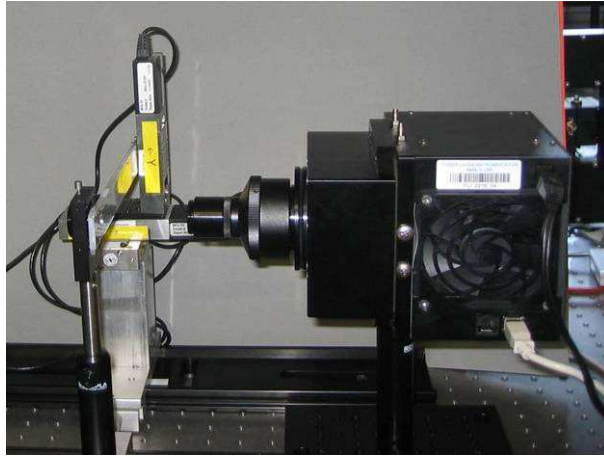
## 4.2 Data acquisition for diffractive imaging

Fourier components for high momentum transfers  $|q|$  correspond to small structures in real space (see section 4.3.3 for more details). The accessible  $q$ -range is determined by the dynamic range of the detector. To improve the resolution of the reconstruction, multiple exposures with acquisition times ranging from 50 ms to 1 min were combined, depending of course on the specific conditions like illumination, investigated sample and use of filters.

Despite all filters, the background counts from stray light were a severe problem in the beginning, especially for long exposure times. The quality of the data improved significantly in a completely darkened room where all possible sources of unwanted light were carefully eliminated. In that configuration



(a) Arrangement of the components along the laser beam.



(b) Detailed view of illumination-defining pinhole, 3D sample translation stage and CCD camera.

**Figure 4.2:** Photos of the laser light setup used for lensless imaging with the PIE technique.

the recorded background became finally independent of the acquisition time. The filters used before turned out to be sources of noise themselves, giving rise to unwanted interferences and reflections. One important factor in this was the design of the CCD detector, which due to its cooling needs an additional glass window in front of the chip (to prevent condensation). Between this glass window and the reflecting surface of the chip interference effects tended to form, disturbing the diffraction pattern. But as the reconstruction did not seem to be too badly affected by this, there was no attempt done to remove the glass window as this could have resulted in severe damage of the CCD.

In a typical data acquisition for PIE, first the exposure times had to be chosen appropriately to allow for a good ‘stitching’ result when combining the images. Besides background (dark) images also the far-field diffraction pattern of the illumination was recorded, see figure 4.3(a) for an example. The diffraction data (figure 4.3(b)) from the sample at overlapping illuminations was collected in a step-by-step mesh scan of the sample with an appropriately chosen step size between the points of the (usually square) grid. At each grid point the desired amount of multiple exposures was taken before moving to the next position. This was chosen above taking consecutive scans for the different exposure times to avoid repositioning errors. The whole mesh scan including this multiple exposure feature was controlled by a self-developed spec macro. Typical scans had  $5 \times 5$  to  $11 \times 11$  points. This depended on

the desired field of view and the chosen step size between adjacent positions. Typically a relative linear overlap of 50–75% was chosen. An overlap of exactly 50% tended to produce artifacts in the reconstruction and also from a geometrical point of view a overlap bigger than 50% seems advisable because then also the next but one neighbours start to overlap.

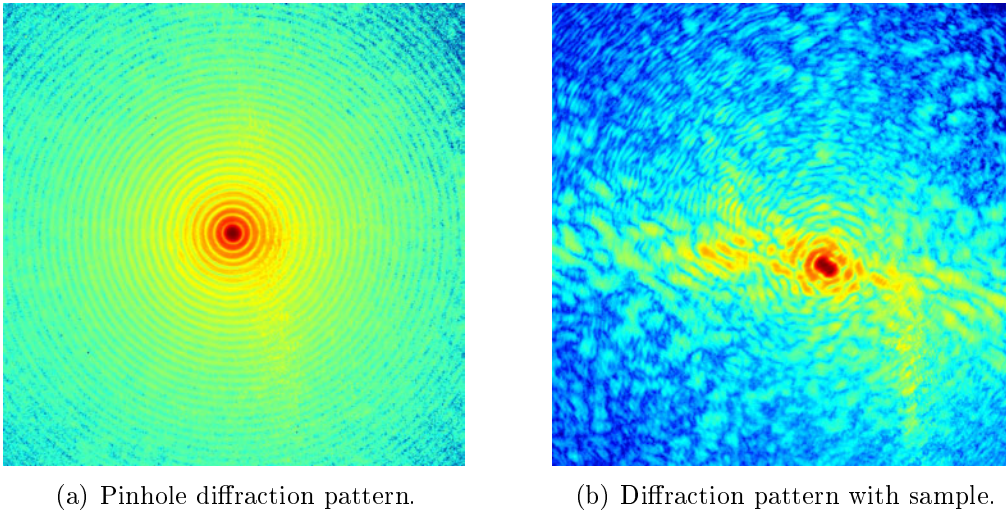


**Figure 4.3:** Typical diffraction patterns (color-coded logarithmic scale) from (a) the illuminating pinhole alone and (b) with sample (the dog flea shown in figure 4.5). While for (a) four exposures ranging from 0.25 s to 20 s were used, for (b) additionally a fifth exposure (30 s) was taken. The pattern (b) is off-centered because the cover-glass on the sample was tilted with respect to the slide below. There is no symmetry with respect to the center indicating that the sample has a complex exit wave.

## 4.3 Processing of experimental data

The PIE algorithm has already been introduced in section 2.3.4. In this section more details of the actual implementation for the reconstruction of experimental data will be discussed.

Like the simulations, all the reconstructions were done with MATLAB.

### 4.3.1 Determination of the illumination function

Recalling what the PIE algorithm uses as input information, we have to provide an accurate knowledge of the complex-valued illumination function and its positions relative to the sample, together with the recorded diffraction data for the Fourier magnitude constraints. The illumination function

was usually obtained from a simple model: A disk, i.e. a circular top-hat function, representing a perfect pinhole was created. A convolution with a narrow Gaussian produced more physical smoothed edges. From this a simulated diffraction pattern was calculated and by comparison with the measured far-field data of the illumination, see figure 4.3(a), the radius of the circular top-hat and its amplitude were adjusted so that the diffraction intensities of model and measurement matched. As the sample could not be placed directly in the pinhole plane, the probe at the sample position was calculated by Fresnel propagating the probe at the pinhole plane to the appropriate distance using equation 3.3. A different approach uses standard phase retrieval techniques (the HIO algorithm, e.g., see section 2.3.3) to reconstruct the illumination function. This is of special interest in cases where modeling the illumination is not easily done [54], like if one wants to include deviations caused by pinhole imperfections. This approach requires diffraction patterns of the probe of rather high quality to get a reconstructed probe that gives PIE reconstructions of quality comparable to the one obtained with a modeled probe. The reason for this is, that the standard phase retrieval algorithm attributes all noise in the probe diffraction pattern to deviations of the pinhole or its illumination from the ideal case. Therefore too much noise from other sources results in unphysical features in the reconstructed probe function. The approach is thus not yet able to provide a way to run a whole PIE reconstruction model independent with only diffraction patterns as input.

A second idea is to improve the probe by feedback from the PIE reconstruction: As the roles of probe and object function can be easily exchanged in the PIE algorithm, with diffraction data from a well-defined object an ‘inversed’ PIE loop can be done. That means, leaving the object fixed and updating only the probe using the redundant information from all positions of the mesh to reconstruct it. When imaging a different object with the same illumination the retrieved probe can then be used for the reconstruction.

Combining both the modeling and the ‘inversed PIE’, one can think of constructing a modified algorithm with a feedback loop for probe refinement, see diagram in figure 4.4: First a reconstruction of the object is done with a modeled probe in a standard PIE loop. Then an ‘inversed’ PIE loop follows, giving an updated version of the probe that can be used to again reconstruct a new object. It is not clear yet, if this approach will lead to converging solutions for both the object and the probe. In first tests with experimental data, the method seemed to reduce artifacts in the reconstructions though this was not true for all data sets. Further studies will have to be carried out to assess the usefulness of the idea.

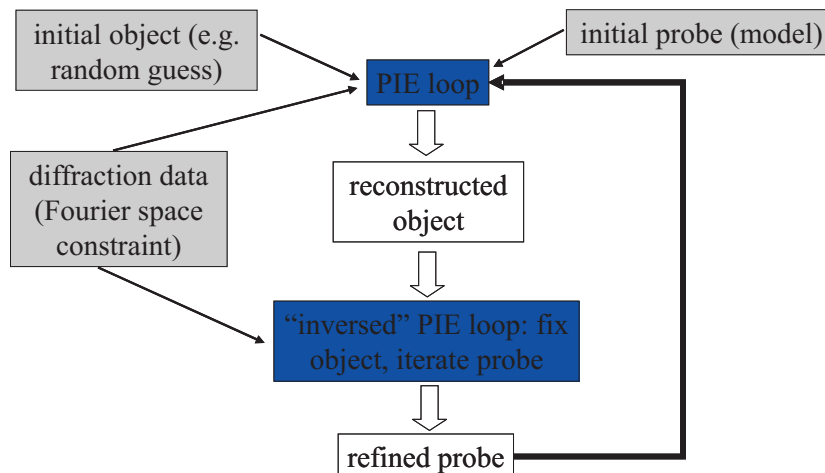


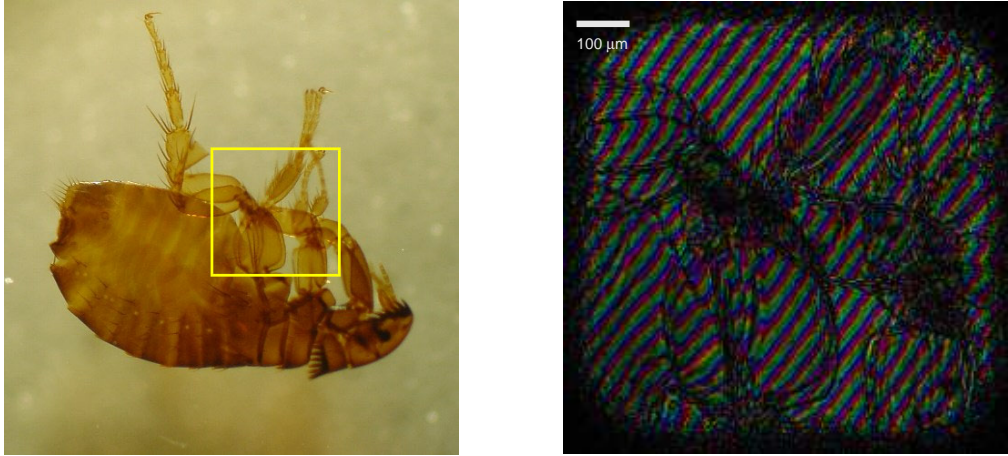
**Figure 4.4:** PIE algorithm with feedback loop for probe refinement: The result of a first reconstruction with a modeled probe is held fixed in an ‘inversed’ PIE loop to reconstruct the probe.

### 4.3.2 PIE processing

The diffraction patterns were imported into MATLAB using a custom-made reading routine for the data format produced by the CCD. The patterns measured with different exposure times were combined by successively substituting all pixels with values above a certain threshold by the corresponding pixels from the next shorter exposure. The data was then cropped to the region where signal was present, because the background noise of pixels at high momentum transfers made the reconstruction unstable. If the diffraction patterns were not well centered within the selected region, compare figure 4.3(b), a linear phase ramp appeared in the reconstructed phase, see equation (2.3). Figure 4.5 shows a rather extreme example for phase wrapping which occurs for large phase ramps because the phase is only given modulo  $2\pi$ . Such phase ramps can then be used to precisely determine the center of the diffraction patterns, assuming that the phase image should have a flat background.

The cropped and centered diffraction patterns were normalized (normalization constant obtained from the modeling parameters of the probe) and the Fourier magnitudes were calculated as the square roots of the intensity values. If the oversampling ratio  $\sigma$  of the data is much higher than 2, the data can be down-sampled (or (re-)binned) to images with less pixels which reduces the computation time without losing information. Of course, the matrix containing the probe has to be corrected to the new size as well.

The size of the matrix representing the object has to be chosen in a way, that it fully contains the probe matrix when the latter is centered over any of



(a) Light microscope image of a dog flea.

(b) PIE reconstruction of framed area.

**Figure 4.5:** Image (a) shows a standard light microscope of a dog flea (prepared slide purchased from Euroslides). The yellow frame marks the area whose reconstruction from a PIE scan is shown in (b). It is a good example for a huge phase ramp in the retrieved phase as a result of translated diffraction patterns. The diffraction patterns (see figure 4.3(b)) were too far off-center to fully correct for it in the reconstruction by shifting the origin.

the positions defined by the scanning mesh. The object is usually initialized with random numbers as a first guess and then the PIE reconstruction starts picking the appropriate part of the object array for each illumination position and applying the algorithm as described in section 2.3.4.

### 4.3.3 Pixel size in reconstructed images

In what follows it is assumed that the diffraction patterns cover the full field-of-view in the recorded (and probably cropped) images and that nothing like zero-padding is done that would alter the pixel size in the retrieved image but not increase the information content. If we define the resolution of the reconstructed image as the minimum distance for which we still can distinguish two adjacent points of the object, we get twice the pixel size for a pixel-based image. We now want to calculate the size of one pixel in the reconstruction:

We have a square CCD chip with a side length  $D = Nd$ , where  $N$  is the number of pixels in a row or column and  $d$  the size of the pixels. From the object plane at distance  $Z$  from the chip, it is then seen under an angle  $\alpha \approx D/Z$  (small angle approximation). With Bragg's law (2.71) in its small angle form  $q = 2k/\theta = k/(2\alpha)$  we can relate this angle to a momentum

transfer

$$Q = 2|\mathbf{q}_{\max}| = \frac{2\pi}{\lambda}\alpha. \quad (4.1)$$

From that the sampling interval in Fourier space  $\Delta q = Q/N$  can be calculated, which is related to the (linear) pixel size  $\Delta x$  in the reconstructed image by equation (2.14). With (4.1) this results in

$$\Delta x = \frac{2\pi}{N\Delta q} = \frac{\lambda}{\alpha}, \quad (4.2)$$

directly showing that the pixel size  $\Delta x$  in the reconstruction is inversely proportional to the maximum angle covered by the detector. With the geometrical values introduced above we get

$$\Delta x = \frac{\lambda Z}{Nd}. \quad (4.3)$$

As the direct measurement of the distance  $Z$  was not easily possible with the required precision, the pixel size was usually determined as the ratio

$$\Delta x = \frac{r_{\text{real}}}{r_{\text{model}}}, \quad (4.4)$$

where  $r_{\text{real}}$  is the known radius (in meter) of the illumination-defining pinhole and  $r_{\text{model}}$  the radius in pixel used in the model. As this latter radius is adjusted by comparison of calculated and measured diffraction patterns, no knowledge of  $Z$  is needed to determine the pixel size. On the contrary, the so determined  $\Delta x$  can be used to calculate  $Z$  with (4.3).

Binning of the diffraction data does not change the resolution of the reconstructed image, as the product  $Nd$  in equation (4.3) remains constant. As long as the sampling condition is fulfilled, binning is equivalent to removing some of the extra zeros around the support of the object.

## 4.4 Reconstructions with different overlap parameters

Quantitative simulations to investigate the influence of the overlap parameter can be found in section 3.1. The terminology defined there will be used in what follows. As one cannot define a reference for the quality of reconstructions of an unknown sample, a similar quantitative assessment cannot be done. We will therefore discuss the results only on a qualitative basis.

The experiments were carried out with a pinhole of 200  $\mu\text{m}$  diameter at a sample-to-detector distance of 20 cm. As test sample a fly wing was used. A

light microscope image of it is shown in figure 4.6(l). The sample was placed 1.5 mm behind the illumination-defining pinhole. The scans had  $11 \times 11$  positions with relative overlaps ranging from 0% to 100%. The reconstructed images are visualized as HSV false color plots in figure 4.6(a)–(k), as usual amplitude coded as brightness and phase as hue. For each of the images 30 PIE iterations were done. The reconstructed images were retrieved with an arbitrary phase offset. As mentioned before this is an inherent feature of iterative phase retrieval techniques. This phase offset has been adjusted in the images in figure 4.6(a)–(k) for ease of comparison.

In figure 4.6(a), i.e., 0% nominal overlap, one sees some slight correlation for the average phases of individual positions. Also some amplitude features are visible. This is probably caused by the overlap of the weak tails of the incident probe due to the free-space propagation from the pinhole to the object plane. With increasing overlap the phase values of adjacent positions become more and more correlated and larger patches start to form in figure 4.6(c). Figure 4.6(d) shows the reconstruction for 30% overlap, the value that was recommended in section 3.1 for fast overview scans and highly radiation sensitive samples. At 60%, which we beforehand found to be the preferable value, the highly absorbing lines of the wing are well defined and artifacts in the background are further reduced, see figure 4.6(g). Increasing the overlap even more yields only little improvement of the image quality at the expense of considerably large overhead in scanning time and higher dose on the sample. When PIE degenerates to a standard iterative phase retrieval algorithm at 100% overlap, figure 4.6(k), an image of very low quality is retrieved although 30 PIE iterations of the  $11 \times 11$  now equivalent positions corresponds to 3630 total iterations for that central area. In summary, the experimental data confirm the results of the simulations discussed in section 3.1.

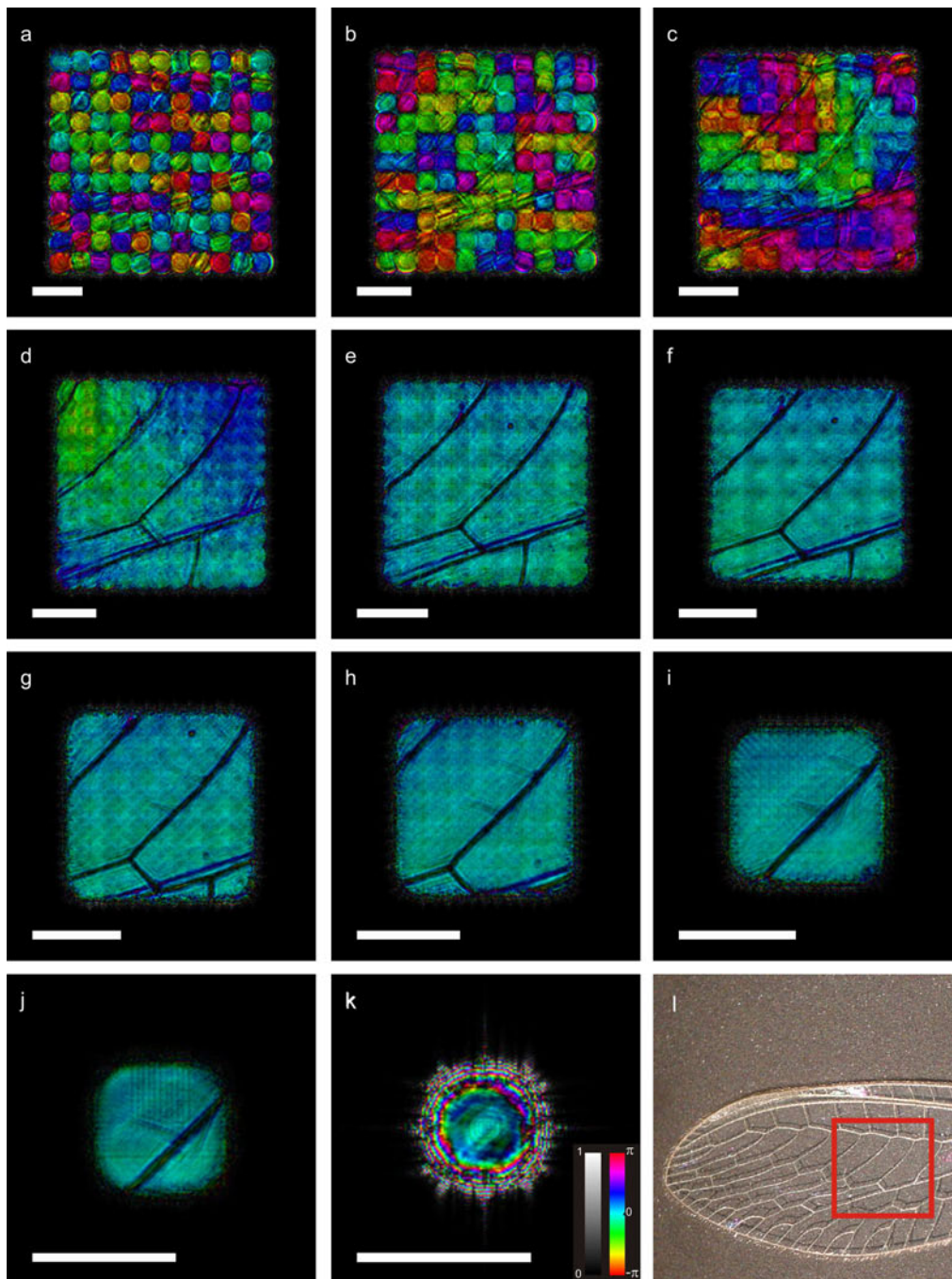


**Figure 4.6:** Reconstructions from measured data sets for different relative overlaps. The relative overlap is increased in steps of 10% from 0% (a) to 100% (k). The white scale bar represents 0.5 mm. The red frame in the light microscope image of the sample (l) marks the region covered in a. Brightness represents amplitude and hue codes phase according to the colorbars in k.

## 4.5 Toward routine lensless imaging applications

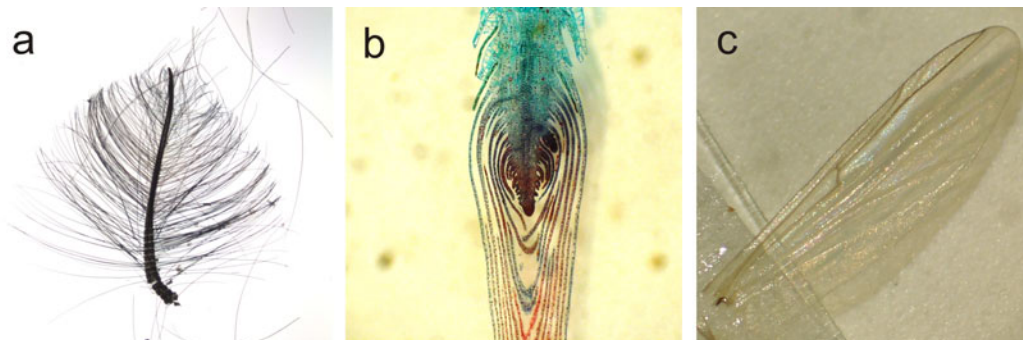


**Figure 4.7:** Standard light microscope images of three samples that were imaged with the laser PIE setup: The insect antenna (a) and the wing (c) were taken from a dead fly belonging to the family of *chironomidae*. (b) is a prepared slide (purchased from Euroslides) with the stem tip of a *hydrilla verticillata*. The corresponding reconstructions are shown in figure 4.8

On a medium-term time scale it would be nice to run coherent diffraction microscopy setups as standard user instruments at synchrotrons.<sup>1</sup> For our laser setup we gradually improved the degree of automation in the reconstruction scripts and thus the user-friendliness. When the geometry of the setup does not change, all that has to be provided are the basic parameters of the scan, like the step size, the number of positions, the number of exposures at each position, and some knowledge about the probe. In the case of a modeled probe, only the radius has to be determined by comparison of modeled and measured diffraction pattern, the normalization constant may be directly obtained from the highest pixel value. In a next step, the scan parameters could also be directly passed from the control software.

The data files of the scan are identified by one single scan number. If multiple exposures are used, the reading routine scales the data appropriately and replaces overexposed pixels without any user interaction required. For the PIE loop itself, one usually has to change only the number of desired iterations.

Of course, too much automation always includes the risk of losing the control over certain parameters or relying too much on the automatically obtained results. So it should firstly be used to automate truly trivial things that do not directly affect the reconstruction process. Only for a very stable and reliable setup with good data one can do further steps toward automation,

---

<sup>1</sup>There may even be a small niche for lensless laser imaging in cases where standard lens systems cannot be used.

like retrieving the probe from its diffraction pattern.

To illustrate that our laser setup can be used for imaging in a routine way,

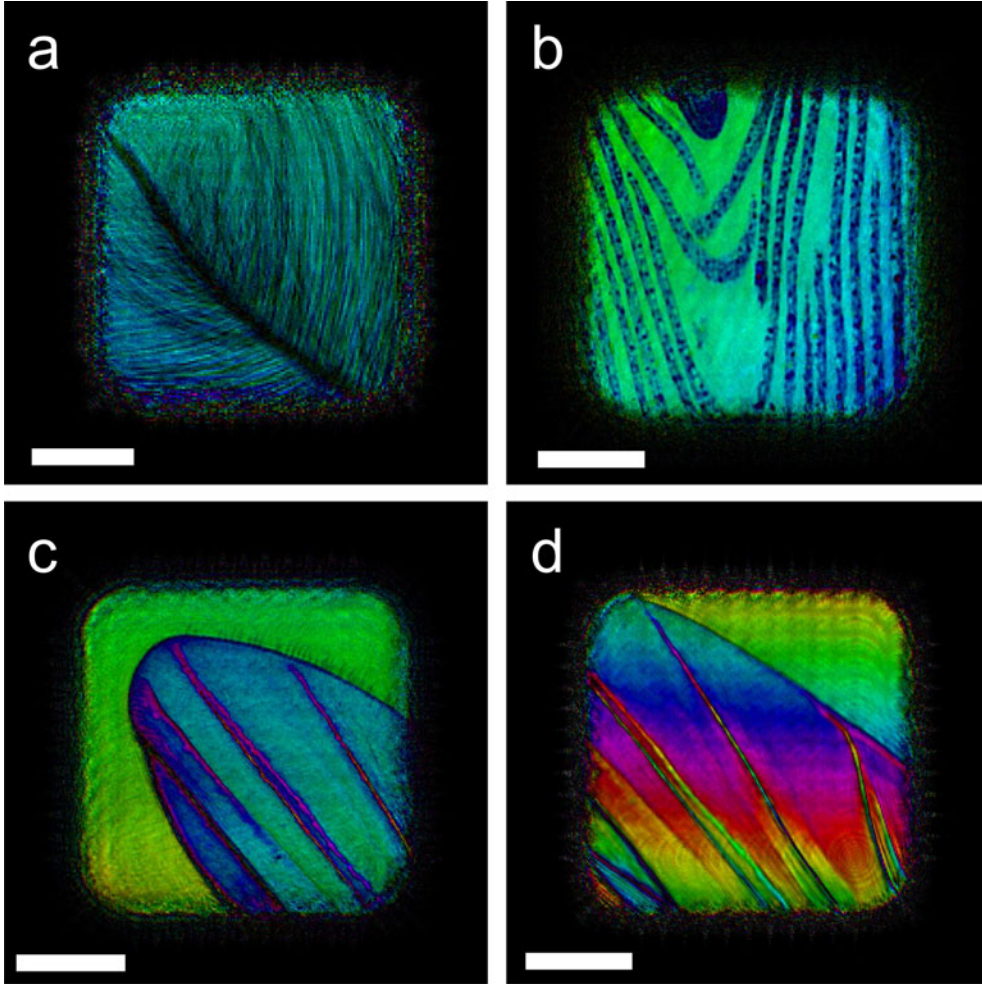


**Figure 4.8:** The labeled images (a)–(c) each show the reconstructions of the objects which have the same label in 4.7. (d) is a high-resolution image of the fly wing in (c). The white scale bar represents 0.25 mm. See text for more details.

reconstructions from the three samples shown in figure 4.7 shall be discussed as representatives. Each of the reconstructions (a)–(d) in figure 4.8 was obtained from a  $11 \times 11$  PIE mesh. For (a) and (d) only a single exposure (at each position) was used, while for (b) and (c) multiple exposures of different lengths were combined. Already the images from single exposures are usually of quite good quality. They can be improved further by multiple exposures so that small details like the hairs at the edge of the wing in (c) become visible. While (a),(c) and (d) were reconstructed from samples that were in air,

(b) is from a prepared slide, where the specimen is confined between a cover glass and a standard microscopy slide. It is one example that showed that the setup had no particular difficulties with the additional glass surfaces (as long as they were parallel and did not introduce additional phase gradients as in figure 4.5(b)).

# Chapter 5

## Diffractive imaging with hard x-rays

### 5.1 Synchrotron radiation

The diffractive imaging x-ray experiments were carried out using synchrotron radiation. A sketch of a synchrotron experiment is shown in figure 5.1, together with some typical distances. The radiation is generated in the insertion device (here an undulator) by oscillations of the electrons that are orbiting in the storage ring. The crystal-monochromator uses Bragg reflections to select a narrow spectral band. Often focusing devices are used before the beam is delivered on the sample.

Some main aspects of the generation of synchrotron radiation will be pointed out, more details and the derivations of the equations can be found in [1]. Different types of x-ray sources can be characterized by their brilliance  $B$

$$B = \frac{\text{photons / second}}{(\text{mrad})^2 (\text{mm}^2 \text{source area}) (0.1\% \text{bandwidth})}. \quad (5.1)$$

The intensity of the beam in photons per second *after* a monochromator can then be calculated as the product of brilliance, angular divergences set by the horizontal and vertical apertures (in milli-radian), the source area (in  $\text{mm}^2$ ) and the bandwidth of the monochromator relative to 0.1%. The *flux* of the source is defined as photons per second per unit area.

#### 5.1.1 Radiation from a circular arc

Synchrotron radiation is produced when electrons at relativistic speed travel along curved trajectories. In a synchrotron the electrons revolve in a storage

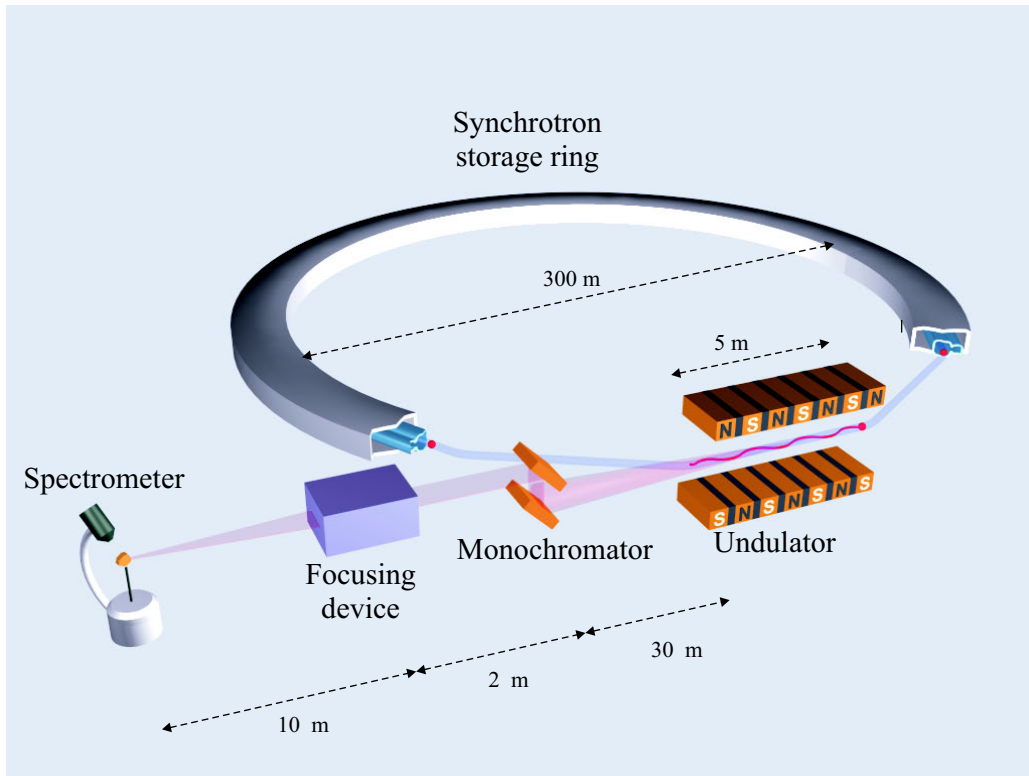


**Figure 5.1:** Sketch of a x-ray experiment at a synchrotron showing major components and the typical distances. From [1].

ring kept on their orbits by bending magnets. An electron of energy  $E_e$ , moving on a circular trajectory at relativistic speed  $v$ , emits radiation into a cone with an opening angle of  $\gamma^{-1} = m_e c^2 / E_e$  ( $m_e$  is the electron mass,  $c$  the vacuum-speed of light). The instantaneous axis of this cone is always parallel to the instantaneous velocity of the electron. This bending magnet radiation has certain properties:

- A very broad (far infrared to hard X-ray) spectrum with hard X-ray cut-off at frequencies of order  $\gamma^3 \omega_0$  ( $\omega_0 =$  cyclic frequency of the orbiting electron).
- On-axis polarization: linear in the horizontal plane.
- Off-axis polarization: right-handed circular above the orbit plane, left-handed circular below.
- Radiation is pulsed with a pulse duration that equals length of electron bunch divided by  $c$ .

The radiated power from a section  $L$  along the electron path at a current  $I$  in the storage ring is given by

$$P[\text{kW}] = 1.266 E_e^2[\text{GeV}] B^2[\text{T}] L[\text{m}] I[\text{A}] . \quad (5.2)$$

### 5.1.2 Insertion devices

At a modern ‘third generation’ synchrotron source the storage ring has several straight sections between the circular arc segments within the bending magnets. In these straight sections so-called *insertion devices* can be operated, like the undulator depicted in figure 5.1. Insertion devices consist of two opposed arrays of magnets which produce a magnetic field alternating from up to down along the path. The electrons oscillate several times and so the radiation from several curved paths adds up. There are two main types of insertion devices, wigglers and undulators. They can be characterized by the maximum angular deviation  $K$  of the electrons from the axis of the device. For undulators  $K$  is usually around 1, as for wigglers it has a value around 20.

#### Wigglers

The trajectory of electrons in a Wiggler can be viewed as a series of circular arcs: The radiated intensities of all arcs add up and thus increase the total intensity by a factor of two times the number of periods. The spectrum is the same as for a bending magnet of the same magnetic field strength.

#### Undulators

Undulators are designed in a way that the radiation emitted by a certain electron at one oscillation is in phase with the radiation from the following oscillations. So the amplitudes of the radiated waves are first added and then the sum is squared to obtain the total intensity. Undulator radiation has a very small bandwidth because the coherent addition of amplitudes is only valid at one particular wavelength and its harmonics. For higher  $K$  values the intensity of the harmonics increases and they are shifted to lower photon energies. As the  $K$  value is proportional to the peak magnetic field, it changes when the gap between the two arrays of magnets is altered. In an experiment the gap can be adjusted to give the best performance for the wavelength selected by the monochromator. The intrinsic angular divergence is much smaller than for wigglers or bending magnets. Undulators can provide enough coherence to make diffractive imaging possible.

## 5.2 Experimental setup

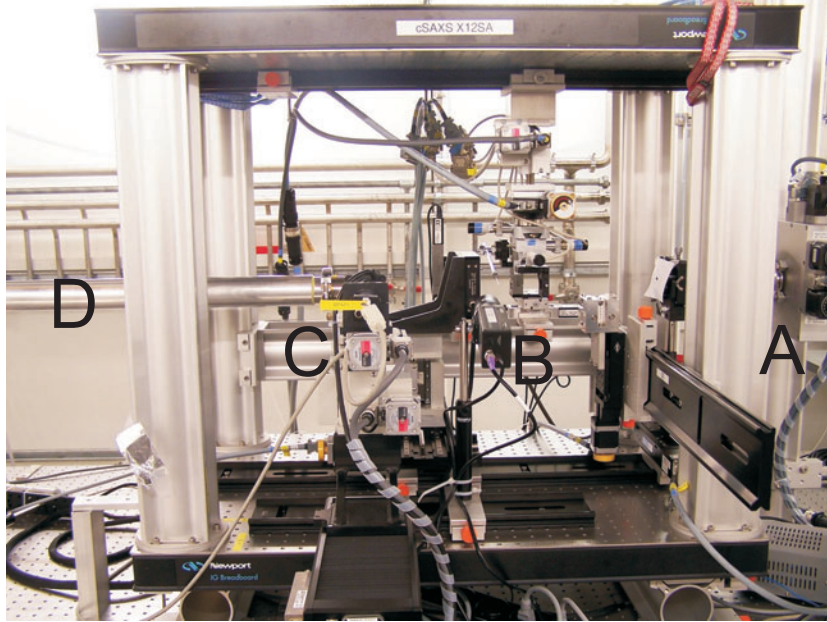


**Figure 5.2:** Overview of the experimental setup used for x-ray diffractive imaging experiments. The labeled components are: Slits (A), illumination-defining pinhole arrangement and sample stage (B) (see also the close-up view in figure 5.3), ‘x-ray eye’ for alignment (C) and the evacuated flight-tube (D) leading towards the detector (not shown here). See text for more details.

The experiment was carried out at the microXAS beamline of the Swiss Light Source (SLS). The x-ray energy was set to 6.0 keV ( $\lambda = 0.207$  nm) with a liquid nitrogen cooled Si(111) double reflection monochromator. The undulator gap was adjusted to shift the third harmonic of the undulator to this energy. The distance from the source to the sample was around 35 m. The size (FWHM) of the undulator source is approximately 202  $\mu\text{m}$  in horizontal and 18  $\mu\text{m}$  in vertical direction. If we assume a Gaussian source and calculate the sigma widths  $\sigma = \text{FWHM}/(2\sqrt{2\ln 2})$  we can obtain an estimate for the transverse coherence lengths with equation (2.52). With the given values we get  $\xi_h \approx 13.4$   $\mu\text{m}$  for the horizontal and  $\xi_v \approx 150$   $\mu\text{m}$ . The illumination on the sample was defined by a pinhole right in front of it with a diameter of 10  $\mu\text{m}$ . We infer that the illumination on the sample was substantially, although not perfectly, spatially coherent. To get a well-defined probe, the size of the beam was first reduced by a pair of slits, figure 5.2 (A). Scattering from the slit blades was removed from the beam by a 100  $\mu\text{m}$  pinhole (Linos) placed behind them, see figure 5.3 (A). Pinhole (B)

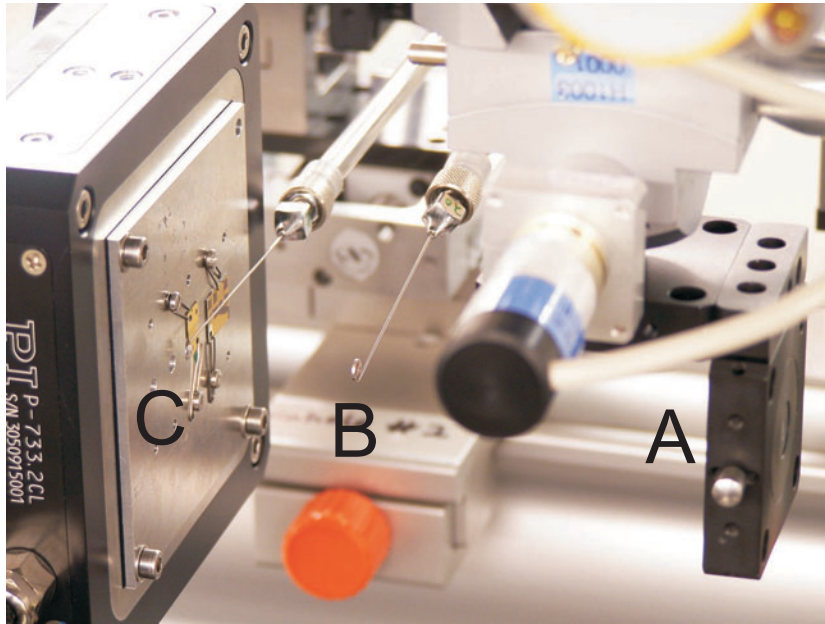
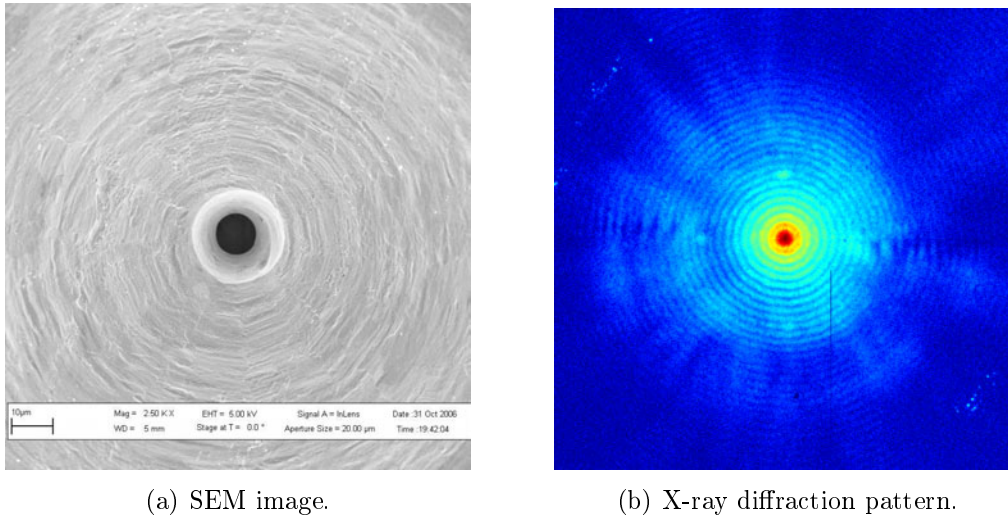


**Figure 5.3:** Illumination-defining pinholes (A,B) and sample stage (C) of the hard x-ray setup. The third pinhole, which is not labeled separately, is as close as possible to the sample. See text for more details.

in figure 5.3 had a diameter of  $20\ \mu\text{m}$ . It was intended to block most of the radiation coming through the  $100\ \mu\text{m}$  aperture, because we observed that still a significant part of the beam would otherwise penetrate through the material around the following  $10\ \mu\text{m}$  aperture. The used pinholes were commercial Pt/Ir apertures for electron microscopy (Plano). To be able to get as close as possible to the sample, the pinholes were spot-welded on syringe needles (visible in figure 5.3, label (B)). Before the experiment several pinholes had been inspected with a scanning electron microscope (SEM). For the best-looking we then compared the x-ray diffraction patterns to choose the one which produced the cleanest illumination. SEM image and diffraction pattern of our final choice are shown in figure 5.4. The pinholes were motorized with different kinds of stepper motors (Newport, Faulhaber) to allow for precise and reproducible alignment.

The samples were mounted on a two-dimensional piezo-driven stage (PI P-733.2DD) with  $100\ \mu\text{m}$  travel range along each axis. The piezo stage was placed on a combination of stepper motor driven stages (Kohzu, Owis) to allow larger movements. For a rough alignment of the beam defining components a laser was adjusted to point along the x-ray beam path. Fine alignment was done directly with the x-ray beam. For this a ‘x-ray eye’ (figure 5.2 (C))



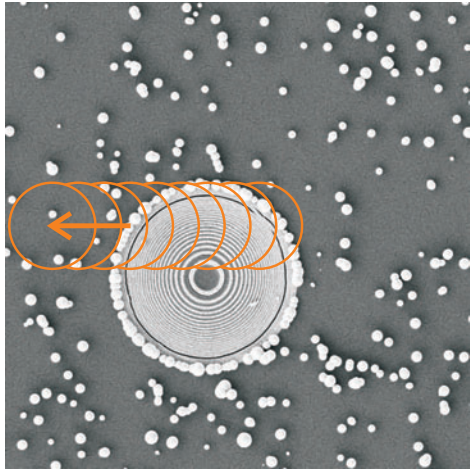
(a) SEM image.

(b) X-ray diffraction pattern.

**Figure 5.4:** SEM image (a) and x-ray diffraction pattern (b) of the 10  $\mu\text{m}$  pinhole used in the x-ray experiment. The diffraction pattern is combined from two acquisitions with exposure times of 0.5 s and 5 s. It is plotted on a color coded logarithmic scale.

was installed. It used a video camera with a microscope objective to image a scintillator which converted the x-rays to visible light. The x-ray eye was also used to find the samples on their supporting structures. Of course, this is only possible if the samples show enough absorption contrast.

The diffraction patterns were recorded with a CCD with fiber-optical scintillator input (Photonic Science Hystar), which had  $2096 \times 2048$  pixels with an effective size of  $4.5 \mu\text{m} \times 4.5 \mu\text{m}$  each. To be able to work in the far-field and to sufficiently oversample the diffraction pattern, the detector was placed about 2.9 m downstream from the sample. For 2.5 m of this distance the beam traveled through an evacuated flight tube, figure 5.2 (C), to avoid absorption and scattering processes in air. The detector had to be connected to an external shutter, so that there was no signal during readout of the chip. The detector software was operated to wait for trigger signals (TTL pulses) from the motor control software, which then caused acquisitions with a predefined exposure time. To increase the dynamic range by combining patterns from different exposure times, several separate PIE scans were done. However, this renders errors due to the potentially insufficient repositioning accuracy (e.g., due to thermal drift) more likely.



(a) SEM image of Fresnel zone plate.



(b) SEM image of PSI logo.

**Figure 5.5:** SEM images of the samples used in the x-ray PIE experiment. The Fresnel zone plate in (a) has a diameter of  $20\ \mu\text{m}$ . The circles indicate the probe positions for which the diffraction patterns in figure 5.6 were recorded. The width of the PSI logo is  $16\ \mu\text{m}$ . Images courtesy of Konstantins Jefimovs.

### 5.3 Investigated samples

We used two different gold nanostructures, a Fresnel zone plate (FZP) and a PSI logo, see figure 5.5. They were fabricated by Konstantins Jefimovs (X-ray Optics and Applications Group, Laboratory for Micro- and Nanotechnology, Paul Scherrer Institut) using electron beam lithography, a series of etching steps and electroplating of gold. Technical details can be found in [39].

The zone plate shown in figure 5.5(a), has a diameter of  $20\ \mu\text{m}$  and the width of its outermost zones is  $100\ \text{nm}$ . The height of the gold structures is around  $1\ \mu\text{m}$ . The substrate supporting the zone plate is a silicon membrane of approximately  $4\ \mu\text{m}$  thickness. The gold balls outside the zone plate range approximately from  $250$  to  $1500\ \text{nm}$  in diameter.

The logo of the Paul Scherrer Institut (PSI) in figure 5.5(b) has a size of  $6\ \mu\text{m} \times 16\ \mu\text{m}$ . It was specially produced for the experiment to have a well-defined structure without the symmetries and periodicities of a zone plate.

Besides these fabricated nanostructures, some tobacco mosaic viruses were available on standard copper grids as used in transmission electron microscopy.

## 5.4 Results

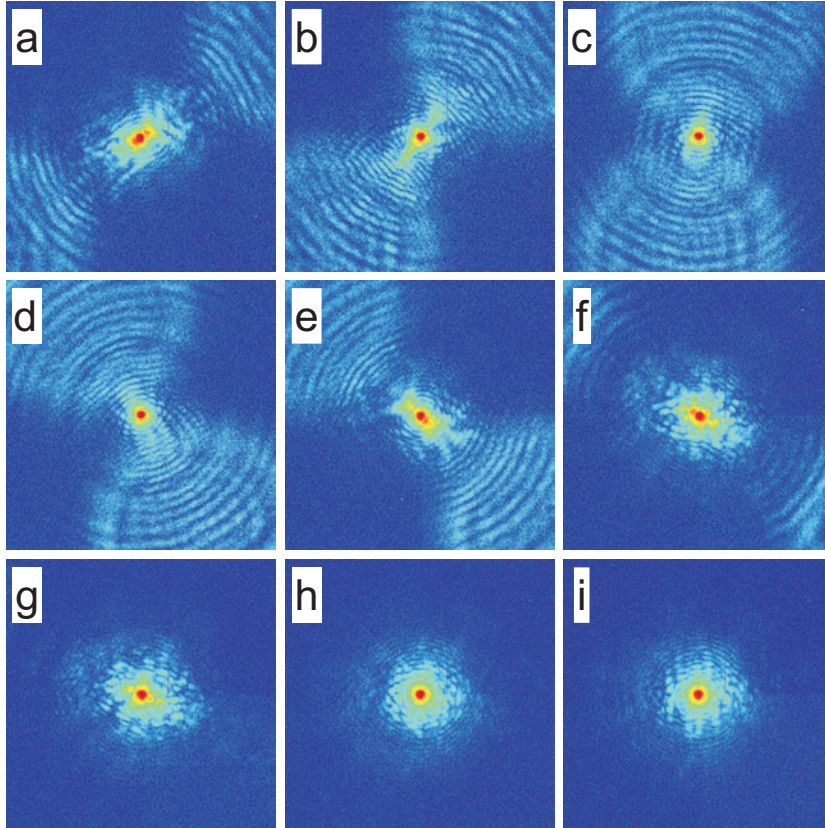


**Figure 5.6:** Central regions of diffraction patterns from the PIE scan of the Fresnel zone plate, plotted on a color-coded logarithmic scale. The exposure time was 1 s. As depicted by the circles in figure 5.5(a), in (a)–(f) the illumination function passes over the zone plate creating a strongly directed diffraction signal that reflects the average orientation of the illuminated structures. In the patterns (g)–(i) from the random gold balls no preferred orientation is visible and just the speckle in the central part change.

The reconstruction procedure was exactly the same as described in section 4.3 for the laser data. The same MATLAB scripts were used with just some slight modifications of the loading procedures. With a modeled illumination function, good reconstructions were obtained, whereas the application of phase retrieval on figure 5.4(b) to reconstruct the probe turned out to be difficult.

As we observed repositioning errors between two scans that were identical except for the exposure times, the reconstructions had to be done with single exposures. This limits the accessible range in Fourier space dramatically, because the acquisition time has to be short enough that the central pixels

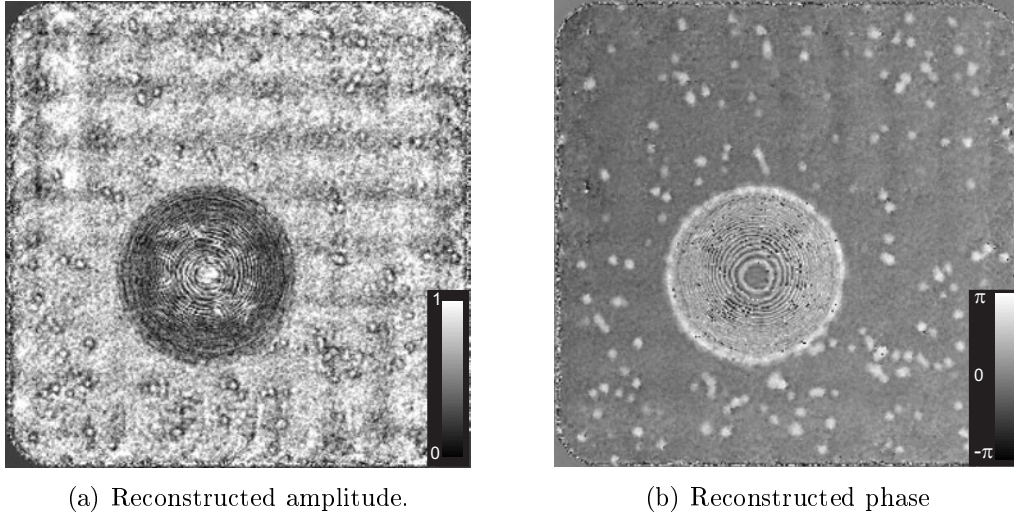


**Figure 5.7:** PIE reconstruction of a gold Fresnel zone plate of  $20\ \mu\text{m}$  diameter. The normalized amplitude of the complex exit wave is shown in (a), the phase in (b). 20 PIE iterations were done on the six-fold binned diffraction data.

do not saturate. For the reconstructions presented in this chapter, the data was thus cropped to  $768 \times 768$  pixels. With our geometry this results in a pixel size of  $\sim 180\ \text{nm}$  in the reconstructed image. With this resolution, the tobacco mosaic viruses could not be resolved. The discussion thus focuses on the imaged nanostructures.

#### 5.4.1 Fresnel zone plate

Data from the membrane with the Fresnel zone plate shown in figure 5.5(a) was taken at  $15 \times 15$  positions with  $3\ \mu\text{m}$  step size. This corresponds to a relative linear overlap of 70% that should – as far as the dependence on the overlap is concerned – allow for a good reconstruction (see section 3.1). Nine of the 225 diffraction patterns are shown in figure 5.6 (compare also to figure 5.5(a)). When the probe illuminates the first zones, this results in the diffraction pattern (a), revealing an average orientation of about  $45^\circ$  with respect to the Cartesian axes. At (c) the zones are mainly oriented horizontally. The sixth pattern (f) shows that the zones now form an angle of  $90^\circ$  with respect to the ones in (a).

The reconstructed complex exit wave of the object obtained from the full data set is shown in figure 5.7 separately for the phase and the amplitude. The diffraction data was binned by a factor of six. The free-space propagation from the pinhole to the sample was set to  $0.5\ \text{mm}$ . 20 PIE iterations were

done.

We observe that the higher sensitivity of the phase shift results in a better contrast. For example, the gold balls at the rim of the zone plate are barely visible in the amplitude image. The other gold balls also do not show much absorption apart from an edge enhancement effect that makes them visible at all. The horizontal and vertical lines in the amplitude image are reconstruction artifacts, which appear not so pronounced in the phase.

Figure 5.8 shows a close-up view of the SEM image of the zone plate together with the corresponding region from the reconstructed phase. The achieved resolution seems only to be limited by the pixel size, there are no other effects visible that spoil it. As only comparably small regions of the diffraction patterns could be used, the resolution can still be significantly improved if data of sufficient quality is recorded at higher diffraction angles. Despite of that, the potential of the technique can already be seen from the results presented here. The intrinsic resolution of our the setup, if only the transmitted intensity would have been monitored, is given by the 10  $\mu\text{m}$  diameter of our aperture. In our reconstruction we can see isolated objects which are more than 50 times smaller (like the black ring from a collapsed zone in the outer region of the zone plate, that is visible as such in both the SEM image (figure 5.8(a)) and the reconstructed phase (figure 5.8(b))). The central ring of the zone plate is distorted in the phase image, indicating some imperfections in the model of the probe, and especially not correcting for deviations of the probe positions from the ideal mesh.

#### 5.4.2 PSI logo

From the membrane with the PSI logo (see SEM image in figure 5.5(b)) diffraction patterns at  $11 \times 11$  positions with a grid spacing of 3  $\mu\text{m}$  were taken. The exposure time was 0.7 s. For the PSI logo, the difference between reconstructed amplitude (figure 5.9(a)) and the retrieved phase (figure 5.9(b)) is even more significant than for the previously discussed zone plate. Yet it is a good example, how a PIE scan can be used to find an object whose position is not exactly known. Although the rough position was aligned with the x-ray eye, it would not have been exact enough for conventional diffractive imaging. This is because in such a case the object has to be placed exactly behind the coherence-defining aperture. For objects with low absorption this is extremely difficult. In our case, the rough positioning was enough to be sure that the object would be totally inside the range of the scan. If already a good enough model for the probe function exists, one can directly reconstruct a certain scan to define the scanning range for the next one. Especially when one is only interested in certain regions of an extended specimen, the PIE

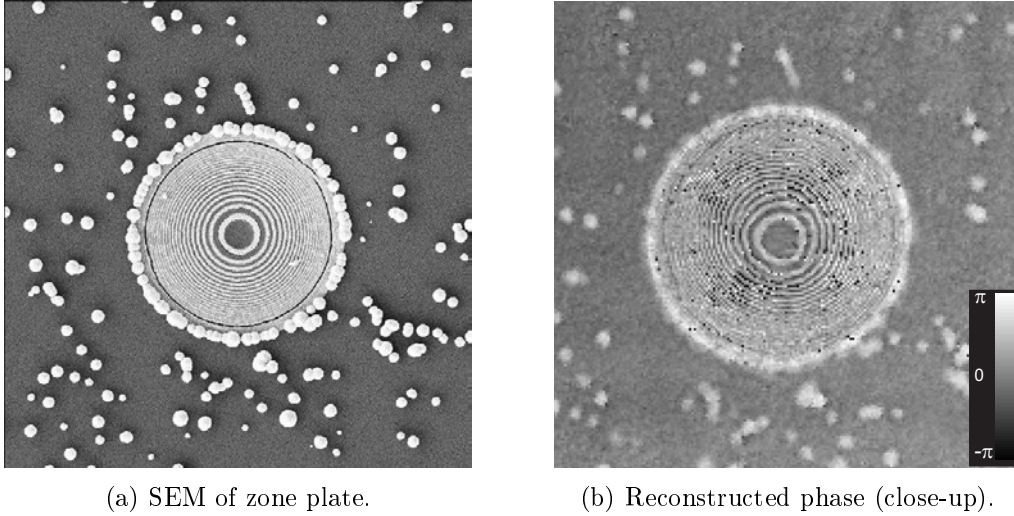


**Figure 5.8:** Detailed view of the zone plate’s SEM image (a) and the corresponding region (b) from the reconstructed phase image. The collapsed zone close to the rim is clearly visible.

algorithm is usually robust enough to get a reasonable image from a fast overview scan that allows to pick out the desired smaller area.

## 5.5 Limitations

Starting from the specific difficulties experienced during the x-ray experiment, we want to discuss some general limitations of x-ray diffractive imaging and possible approaches to deal with them:

- **Stability:**

With the setup described in section 5.2, certain stability problems were observed. Long overnight scans suffered from a drift of sample and optical components, most likely due to thermal expansions. On a shorter time scale, vibrations of the syringe needles holding the pinholes were identified as the most likely reason for some errors. These vibrations were probably caused by the air flowing down from the air conditioning of the x-ray hutch, which was mounted at the ceiling.

In general, due to the small length scales, x-ray diffractive imaging experiments are very sensitive to instabilities of the setup, which should be considered when designing an experiment. For our specific stability issues, replacement of the needles by more stable pinhole mounts and a more compact setup are strategies to cope with the problems.

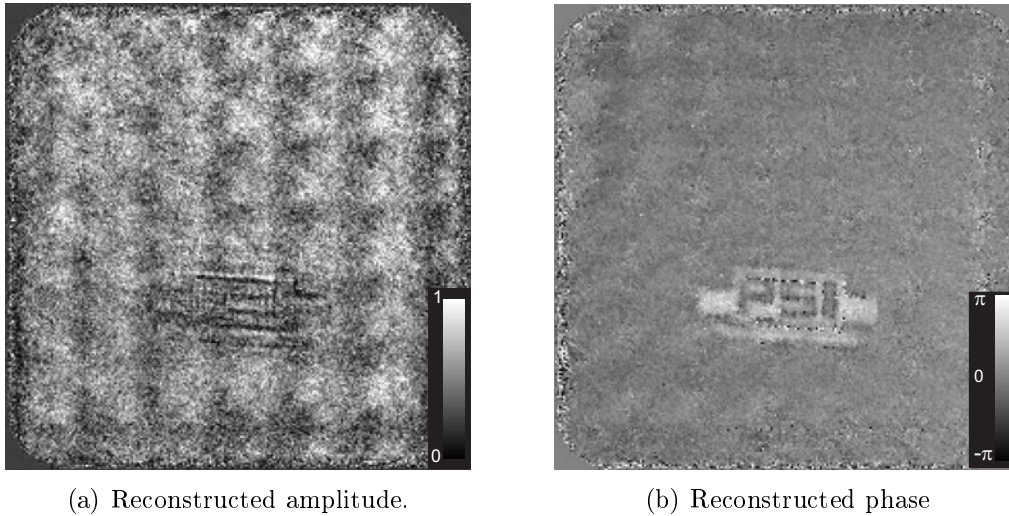


**Figure 5.9:** PIE reconstruction of a  $6\ \mu\text{m} \times 16\ \mu\text{m}$  PSI logo (gold nanostructure). The amplitude is plotted in (a), the phase in (b). The reconstruction was obtained within 10 PIE iterations from the six-fold binned diffraction data.

- **Quality of illumination-defining components:**

Already small imperfections of the illumination-defining pinholes can significantly distort the probe function. Although the pinhole looks nice in the SEM image in figure 5.4(a), its diffraction pattern is far from perfect, see figure 5.4(b). The modeling of such imperfections is usually quite challenging. Phase retrieval methods also tend to fail, because they may, for example, wrongly attribute effects from radiation transmitted through the surrounding material to the hole itself. So it is advantageous to have good probe-defining components. Taking diffraction patterns from various pinholes, we finally made the best experience with pinholes that had been produced or corrected with a focused-ion beam (FIB). Pinholes produced in-house with standard nano-structuring techniques usually had the problem that the material was not opaque enough.

- **High accuracy of positioning:**

Usually the required positioning accuracy can be routinely realized with piezo-driven devices. However, this limits the scan range and may prove to be difficult when a special sample environment has to be moved in and out of the beam.

- **Detection:**

In our case, the achieved resolution was limited by the dynamic range of the detector, as we could not record sufficient data at higher diffraction angles without saturating the central part of the CCD. One method, which was used to record high-resolution data, is to block the central part of the beam. However, the missing central data will probably cause difficulties in the reconstruction process [64, 65]. If one has the possibility to combine diffraction patterns of different exposure times, the blocked area can be replaced with data from a shorter exposure. In our case, combining of multiple images was unfortunately not possible due to misplacement problems with consecutive scans. Other methods to increase the dynamic range would be the use of a semitransparent beam stop or a detector with an increasing sensitivity for higher angles. Besides a high dynamic range, the intrinsic noise level of the detector should be low. Short readout times would allow for faster scans and thus minimize the effects of long-term drifts. In our case the readout time of the CCD was almost ten seconds and thus ten times longer than the actual acquisition times.

- **Radiation damage:**

Biological samples are subject to radiation damage. Therefore the dose a sample can sustain before undergoing significant changes is a limiting factor of the resolution that can be obtained [34]. Besides an appropriate choice of the scanning parameters, namely the overlap (section 3.1.4) and the exposure time, the sample preparation and handling are also important. Cryo-cooling, for example, could be used to significantly reduce the radiation damage [4].

- **Coherence:**

The degree of coherence of the x-ray beam from current synchrotron sources limits the area that can be illuminated at once. Hence only a small part of beam can be used. This limitation can be overcome with energy recovery LINACs (ERL), linear accelerators that provide higher coherence due to a smaller source size. For diffractive imaging with single diffraction patterns, the new generation of x-ray sources, the so-called free-electron lasers (FEL) could be used in future. They provide a fully coherent beam. Apart from the existing soft x-ray FEL FLASH [25], hard x-ray machines are under construction, e.g., the Linac Coherent Light Source (LCLS) in Stanford [41] and the European XFEL in Hamburg [15].

# Chapter 6

## Conclusions and outlook

With this work we have demonstrated the potential of the Ptychographical Iterative Engine (PIE) for lensless coherent imaging. The algorithm has proven its theoretically predicted robustness and uniqueness in several experiments with data sets of different quality. In terms of applications the most significant advantage is the extension of the field of view. PIE provides the possibility to overcome the other algorithm's limitation to isolated objects. This simplifies sample preparation and facilitates its use as a routine imaging method in, e.g., biology and material science.

Our studies of the influence of the overlap parameter on the convergence of the algorithm revealed that scans with smaller step sizes generally yield better reconstructions. However, we found out that radiation sensitive samples should be scanned with a relative linear overlap of  $\sim 60\%$  to achieve good image quality without neglecting the dose delivered to the sample. The convergence was observed to be fast, usually less than 50 PIE iterations are sufficient.

The laser light experiments proved to be useful tools to test certain parameters of the method. The capabilities and the phase retrieval scripts were gradually improved with the increasing needs for more sophisticated processing schemes. However, phase retrieval techniques for reconstructing the probe from measured data and thus making the method model-independent did only work with very good data sets.

Due to experimental limitations the x-ray data could not provide ultimate resolution. The reconstructions were nevertheless showing a considerable amount of details. The limiting factors could be identified and will allow to improve the design of the setup for projected follow-up experiments in the near future.

For the further development of the technique we also started to assess combinations with other existing imaging methods. PIE was mentioned in

section 2.3.3 to be one of two approaches to overcome certain limits of the standard phase retrieval algorithms. The other approach, *Fresnel Coherent Diffractive Imaging* (FCDI, see [51, 53]), uses well-defined wavefront curvatures to improve convergence and ensure uniqueness of solutions. With our laser setup we recently implemented the possibility to flexibly illuminate with either a (diverging) curved or a plane wave and to detect either in the near or the far-field. A diverging wave is easily realized with a small pinhole acting as a point source. The plane wave can then be constructed adding a lens that parallelizes the light. A second lens behind the sample ensures that a far-field pattern is detected. When the second lens is removed, we record a near-field diffraction pattern. In the reconstruction code, the different cases are just characterized by two scalar numbers specifying the amount of phase curvature. The four different possible combinations of illumination and detection schemes will be investigated in the near future.

In principle, such a curved wavefront approach can also be transferred to the x-ray case. For example, Williams et al. [67] produced curved x-ray wavefronts with Fresnel zone plate optics. Of course, this can also be combined with PIE. In a very recent first test experiment, gold nanostruc-

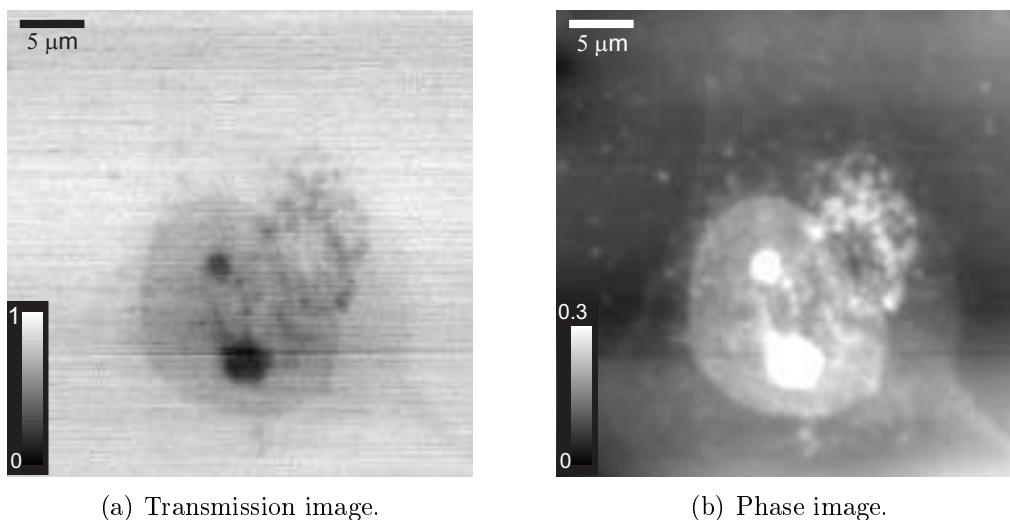


**Figure 6.1:** Transmission (a) and phase (b) of a cytoskeleton specimen prepared from human pancreatic cancer cells. Contrast was enhanced by staining with uranyl acetate and osmium tetroxide. The images are preliminary results from a  $200 \times 200$  mesh with 200 nm step size and 30 ms exposure time. Courtesy of Pierre Thibault.

tures and cytoskeleton-samples (prepared at the Institute of Experimental Physics, Ulm University) could already be measured using this approach. The first preliminary evaluation of the data is shown in figure 6.1. It is no

super-resolution yet, but has the intrinsic 200 nm pixel size from the points of the PIE scan, calculated from looking at integral values of the recorded frames. As the data was recorded with the new PILATUS 2M pixel detector, which has 20 bit dynamic range, no dark counts and a read-out time as fast as 10 ms [35, 36], also large scans of, e.g.,  $200 \times 200$  illumination positions can be recorded in a reasonable amount of time. Fast overview scans, processed to get standard transmission microscopy images, give new possibilities of locating regions-of-interest.

Even without final reconstructions one can already tell from the recorded diffraction data that this approach has a huge potential. A step towards tomography may also be done in the near future.

# Bibliography

- [1] J. Als-Nielsen and D. McMorrow. *Elements of modern X-ray physics*. Wiley, New York, 2001.
- [2] R. H. T. Bates. Fourier phase problems are uniquely solvable in more than one dimension. 1. Underlying theory. *Optik*, 61(3):247–262, 1982.
- [3] H. H. Bauschke, P. L. Combettes, and D. R. Luke. Phase retrieval, error reduction algorithm, and Fienup variants: a view from convex optimization. *J. Opt. Soc. Am. A*, 19(7):1334–1345, July 2002.
- [4] T. Beetz. *Soft X-ray diffraction imaging with and without lenses and radiation damage studies*. PhD thesis, Stony Brooks University, 2004.
- [5] M. Born and E. Wolf. *Principles of optics: electromagnetic theory of propagation, interference and diffraction of light*. Cambridge Univ. Press, Cambridge, 7. edition, 2006.
- [6] R. N. Bracewell. *The Fourier transform and its applications*. McGraw-Hill series in electrical engineering : Circuits and systems. McGraw-Hill, New York, 2. edition, 1986.
- [7] O. Bunk, M. Dierolf, S. Kynde, I. Johnson, O. Marti, and F. Pfeiffer. Influence of the overlap parameter on the convergence of the ptychographical iterative engine. *Ultramicroscopy*, in press, 2007.
- [8] T. Butz. *Fourier transformation for pedestrians*. Springer, Berlin, 2006.
- [9] D. C. Champeney. *Fourier transforms and their physical applications*. Techniques of physics 1. Academic Press, London, 1973.
- [10] H. N. Chapman. Phase-retrieval X-ray microscopy by Wigner-distribution deconvolution. *Ultramicroscopy*, 66(3-4):153–172, Dec. 1996.

- [11] H. N. Chapman, A. Barty, M. J. Bogan, S. Boutet, M. Frank, S. P. Hau-Riege, S. Marchesini, B. W. Woods, S. Bajt, W. H. Benner, R. A. London, E. Plonjes, M. Kuhlmann, R. Treusch, S. Dusterer, T. Tschentscher, J. R. Schneider, E. Spiller, T. Moller, C. Bostedt, M. Hoener, D. A. Shapiro, K. O. Hodgson, D. van der Spoel, F. Burmeister, M. Bergh, C. Caleman, G. Huldt, M. M. Seibert, F. R. N. C. Maia, R. W. Lee, A. Szoke, N. Timneanu, and J. Hajdu. Femtosecond diffractive imaging with a soft-X-ray free-electron laser. *Nature Phys.*, 2(12):839–843, Dec. 2006.
- [12] J. W. Cooley and J. W. Tukey. An algorithm for machine calculation of complex Fourier series. *Math. Comput.*, 19(90):297–301, 1965.
- [13] V. Elser. Phase retrieval by iterated projections. *J. Opt. Soc. Am. A*, 20(1):40–55, Jan. 2003.
- [14] V. Elser, I. Rankenburg, and P. Thibault. Searching with iterated maps. *Proc. Natl. Acad. Sci. USA*, 104(2):418–423, Jan. 2007.
- [15] European XFEL project, Hamburg. <http://xfel.desy.de/>.
- [16] H. M. L. Faulkner and J. M. Rodenburg. Movable aperture lensless transmission microscopy: a novel phase retrieval algorithm. *Phys. Rev. Lett.*, 93:023903, 2004.
- [17] H. M. L. Faulkner and J. M. Rodenburg. Error tolerance of an iterative phase retrieval algorithm for moveable illumination microscopy. *Ultramicroscopy*, 103:153–164, 2005.
- [18] J. R. Fienup. Reconstruction of an object from the modulus of its Fourier transform. *Opt. Lett.*, 3(1):27–29, 1978.
- [19] J. R. Fienup. Phase retrieval algorithms - a comparison. *Appl. Opt.*, 21(15):2758–2769, 1982.
- [20] J. R. Fienup. Reconstruction of a complex-valued object from the modulus of its Fourier transform using a support constraint. *J. Opt. Soc. Am. A*, 4(1):118–123, Jan. 1987.
- [21] J. R. Fienup. Invariant error metrics for image reconstruction. *Appl. Opt.*, 36(32):8352–8357, Nov. 1997.
- [22] J. R. Fienup. Lensless coherent imaging by phase retrieval with an illumination pattern constraint. *Opt. Express*, 14:498, 2006.

- [23] J. R. Fienup, T. R. Crimmins, and W. Holsztynski. Reconstruction of the support of an object from the support of its autocorrelation. *J. Opt. Soc. Am.*, 72(5):610–624, 1982.
- [24] J. R. Fienup and C. C. Wackerman. Phase-retrieval stagnation problems and solutions. *J. Opt. Soc. Am. A*, 3(11):1897–1907, Nov. 1986.
- [25] FLASH, Hamburg. <http://flash.desy.de/>.
- [26] G. R. Fowles. *Introduction to modern optics*. Dover, New York,
- [27] R. W. Gerchberg and W. O. Saxton. A practical algorithm for determination of phase from image and diffraction plane pictures. *Optik*, 35(2):237–246, 1972.
- [28] J. W. Goodman. *Introduction to Fourier Optics*. Roberts & Company, Englewood, Colorado, 3rd edition, 2005.
- [29] M. Guizar-Sicairos and J. C. Gutierrez-Vega. Computation of quasi-discrete Hankel transforms of integer order for propagating optical wave fields. *J. Opt. Soc. Am. A*, 21:53–58, 2004.
- [30] R. Hegerl and W. Hoppe. Dynamische Theorie der Kristallstrukturanalyse durch Elektronenbeugung im inhomogenen Primärstrahlwellenfeld. *Berichte der Bunsen-Gesellschaft*, 74(11):1148–1154, 1970.
- [31] W. Hoppe. Beugung im inhomogenen Primärstrahlwellenfeld. I. Prinzip einer Phasenmessung von Elektronenbeugungsinterferenzen. *Acta Cryst. A*, 25:495, 1969.
- [32] W. Hoppe. Beugung im inhomogenen Primärstrahlwellenfeld. III. Amplituden- und Phasenbestimmung bei unperiodischen Objekten. *Acta Cryst. A*, 25:508, 1969.
- [33] W. Hoppe. Trace Structure-Analysis, Ptychography, Phase Tomography. *Ultramicroscopy*, 10(3):187–198, 1982.
- [34] M. R. Howells, T. Beetz, H. N. Chapman, C. Cui, J. M. Holton, C. J. Jacobsen, J. K. E. Lima, S. Marchesini, H. Miao, D. Sayre, D. A. Shapiro, and J. C. H. Spence. An assessment of the resolution limitation due to radiation-damage in x-ray diffraction microscopy. *arXiv:physics/0502059*, Feb. 2005.
- [35] <http://pilatus.web.psi.ch>.

- [36] <http://sls.web.psi.ch/view.php/beamlines/cs/>.
- [37] Invitrogen Corporation. <http://www.invitrogen.de>.
- [38] J. D. Jackson. *Classical electrodynamics*. Wiley, New York, 14. print edition, 1962.
- [39] K. Jefimovs, O. Bunk, F. Pfeiffer, D. Grolimund, J. F. van der Veen, and C. David. Fabrication of Fresnel zone plates for hard X-rays. *Microelectron. Eng.*, 84(5-8):1467–1470, 2007.
- [40] W. Lauterborn, T. Kurz, and M. Wiesenfeldt. *Coherent optics : fundamentals and applications*. Springer, Berlin, 1995.
- [41] Linac Coherent Light Source (LCLS), Stanford. <http://www-ssl.slac.stanford.edu/lcls/>.
- [42] E. H. Linfoot. *Fourier methods in optical image evaluation*. The Focal library. Focal, London [u.a.], 1964.
- [43] L. Mandel and E. Wolf. Coherence properties of optical fields. *Rev. Mod. Phys.*, 37(2):231–284, 1965.
- [44] S. Marchesini. A unified evaluation of iterative projection algorithms for phase retrieval. *Rev. Sci. Instrum.*, 78(1):011301, Jan. 2007.
- [45] S. Marchesini, H. He, H. N. Chapman, S. P. Hau-Riege, A. Noy, M. R. Howells, U. Weierstall, and J. C. H. Spence. X-ray image reconstruction from a diffraction pattern alone. *Phys. Rev. B*, 68(14):140101, Oct. 2003.
- [46] K. Meyberg and P. Vachenauer. *Höhere Mathematik*, volume 2. Springer, Berlin ; Heidelberg, 3. rev. edition, 1999.
- [47] J. Miao, P. Charalambous, J. Kirz, and D. Sayre. Extending the methodology of X-ray crystallography to allow imaging of micrometre-sized non-crystalline specimens. *Nature*, 400:342–344, 1999.
- [48] J. Miao and D. Sayre. On possible extensions of X-ray crystallography through diffraction-pattern oversampling. *Acta Cryst. A*, 56:596–605, Nov. 2000.
- [49] J. Miao, D. Sayre, and H. N. Chapman. Phase retrieval from the magnitude of the Fourier transforms of nonperiodic objects. *J. Opt. Soc. Am. A*, 15(6):1662–1669, June 1998.

- [50] P. D. Nellist, B. C. McCallum, and J. M. Rodenburg. Resolution beyond the information limit in transmission electron-microscopy. *Nature*, 374(6523):630–632, Apr. 1995.
- [51] K. A. Nugent, A. G. Peele, H. N. Chapman, and A. P. Mancuso. Unique phase recovery for nonperiodic objects. *Phys. Rev. Lett.*, 91(20):203902, Nov. 2003.
- [52] F. Pfeiffer, O. Bunk, C. Schulze-Briese, A. Diaz, T. Weitkamp, C. David, J. F. van der Veen, I. Vartanyants, and I. K. Robinson. Shearing interferometer for quantifying the coherence of hard x-ray beams. *Phys. Rev. Lett.*, 94(16):164801, Apr. 2005.
- [53] H. M. Quiney, K. A. Nugent, and A. G. Peele. Iterative image reconstruction algorithms using wave-front intensity and phase variation. *Opt. Lett.*, 30(13):1638–1640, July 2005.
- [54] H. M. Quiney, A. G. Peele, Z. Cai, D. Paterson, and K. A. Nugent. Diffractive imaging of highly focused X-ray fields. *Nature Phys.*, 2(2):101–104, Feb. 2006.
- [55] P. Reineker, M. Schulz, and B. M. Schulz. *Theoretische Physik*, volume 2: Elektrodynamik. Wiley-VCH, Weinheim, 2006.
- [56] J. M. Rodenburg and R. H. T. Bates. The theory of superresolution electron-microscopy via Wigner-distribution deconvolution. *Phil. Trans. R. Soc. Lond. A*, 339(1655):521–553, June 1992.
- [57] J. M. Rodenburg and H. M. L. Faulkner. A phase retrieval algorithm for shifting illumination. *Appl. Phys. Lett.*, 85:4795–4797, 2004.
- [58] J. M. Rodenburg, A. C. Hurst, and A. G. Cullis. Transmission microscopy without lenses for objects of unlimited size. *Ultramicroscopy*, 107:227–231, 2006.
- [59] J. M. Rodenburg, A. C. Hurst, A. G. Cullis, B. R. Dobson, F. Pfeiffer, O. Bunk, C. David, K. Jefimovs, and I. Johnson. Hard X-ray lensless imaging of extended objects. *Phys. Rev. Lett.*, 98:034801, 2007.
- [60] D. Sayre. Some implications of a theorem due to Shannon. *Acta Cryst.*, 5:843, 1952.
- [61] C. E. Shannon. Communication in the presence of noise. *Proc. Inst. Radio Eng.*, 37(1):10–21, 1949.

- [62] D. Shapiro, P. Thibault, T. Beetz, V. Elser, M. Howells, C. Jacobsen, J. Kirz, E. Lima, H. Miao, A. M. Neiman, and D. Sayre. Biological imaging by soft x-ray diffraction microscopy. *Proc. Natl. Acad. Sci. USA*, 102(43):15343–15346, 2005.
- [63] J. C. H. Spence, U. Weierstall, and M. Howells. Phase recovery and lensless imaging by iterative methods in optical, X-ray and electron diffraction. *Phil. Trans. R. Soc. Lond. A*, 360(1794):875–895, May 2002.
- [64] P. Thibault. *Algorithmic methods in diffraction microscopy*. PhD thesis, Cornell University, August 2007.
- [65] P. Thibault, V. Elser, C. Jacobsen, D. Shapiro, and D. Sayre. Reconstruction of a yeast cell from X-ray diffraction data. *Acta Cryst. A*, A62:248–261, 2006.
- [66] F. van der Veen and F. Pfeiffer. Coherent x-ray scattering. *J. Phys. Cond. Matt.*, 16(28):5003–5030, 2004.
- [67] G. J. Williams, H. M. Quiney, B. B. Dhal, C. Q. Tran, K. A. Nugent, A. G. Peele, D. Paterson, and M. D. de Jonge. Fresnel coherent diffractive imaging. *Phys. Rev. Lett.*, 97(2):025506, July 2006.
- [68] L. Yu, M. C. Huang, M. Z. Chen, W. Z. Chen, W. D. Huang, and Z. Z. Zhu. Quasi-discrete Hankel transform. *Opt. Lett.*, 23(6):409–411, Mar. 1998.

# List of Figures

2.1	Derivation of transverse coherence length . . . . .	17
2.2	Derivation of longitudinal coherence length . . . . .	18
2.3	Illustration of the importance of Fourier phases . . . . .	19
2.4	Schematic representation of the Gerchberg-Saxton / error-reduction algorithm . . . . .	23
2.5	PIE data collection . . . . .	27
2.6	Schematic representation of the PIE algorithm . . . . .	29
3.1	Hue-brightness encoding of complex images . . . . .	32
3.2	Reconstructions of simulated data for different relative overlaps	35
3.3	Error in PIE reconstruction dependent on overlap parameter . .	37
4.1	Laser PIE setup: schema. . . . .	39
4.2	Laser PIE setup: photos. . . . .	40
4.3	Examples of laser light diffraction patterns with and without sample . . . . .	41
4.4	PIE with probe feedback . . . . .	43
4.5	Example for a huge phase ramp in the reconstruction . . . . .	44
4.6	PIE reconstructions with different overlap . . . . .	47
4.7	Samples used for laser PIE experiments . . . . .	48
4.8	Reconstructions from laser PIE data . . . . .	49
5.1	Sketch of a x-ray experiment at a synchrotron . . . . .	52
5.2	Hard x-ray setup for PIE experiments: overview . . . . .	54
5.3	Hard x-ray setup for PIE experiments: detailed view . . . . .	55
5.4	Pinhole used in x-ray experiment: SEM image and diffraction pattern . . . . .	56
5.5	SEM images of Fresnel zone plate and PSI logo used as samples	57
5.6	X-ray PIE data: diffraction patterns from scanning a zone plate	58
5.7	PIE reconstruction of Fresnel zone plate . . . . .	59
5.8	Reconstructed phase and SEM image of Fresnel zone plate . .	61
5.9	PIE reconstruction of PSI logo . . . . .	62

6.1 Preliminary results for a cytoskeleton sample . . . . . 65

# Appendix A

## MATLAB code for a basic PIE simulation

In the code below a RGB image is translated to a complex matrix representation (using the usual hue-brightness coding scheme introduced in section 3). Diffraction patterns are calculated from four different illumination positions with variable overlap and then the object is retrieved using the PIE algorithm.

```
1 clear;
2
3 %% parameters
4
5 r = 40;           %% radius of aperture
6 apshift = 10;    %% half distance between the aperture positions
7 n = 30;          %% number of pie loops
8 alpha = 0.0001;
9 beta = 1;
10 phiobjoffset= 0*pi;
11 dfpatterfignon = 1;
12
13 %% load image data
14 %% fluorescence image of cell, e.g. from www.invitrogen.com
15 %% or http://rsb.info.nih.gov/ij/images/FluorescentCells.jpg
16 %% Image resized to 201x201 pixel
17
18 fluo_cell = imread('cell2.tif');
19 fluo_cell_hsv = rgb2hsv(fluo_cell);
20 datamp = squeeze(fluo_cell_hsv(:,:,3));
21 datphase = 2*pi.*squeeze(fluo_cell_hsv(:,:,1))-pi;
22 dat = flipud(datamp.*exp(sqrt(-1)*datphase));
```

```

23
24 %% define the 4 positions
25 [x,y] = meshgrid(1:201,1:201);
26 xp(1) = 100-apshift; xp(2) = 100-apshift;
27 xp(3) = 100+apshift; xp(4) = 100+apshift;
28 yp(1) = 100-apshift; yp(2) = 100+apshift;
29 yp(3) = 100+apshift; yp(4) = 100-apshift;
30
31 %% model illumination functions (pinhole)
32 for i = 1:4
33     probe(:,:,i) = sign(real(sqrt(r.^2-(x-xp(i)).^2-(y-yp(i)).^2)));
34 end
35
36 %% create diffraction patterns
37 for i = 1:4
38     sim(:,:,i) = (fft2(squeeze(probe(:,:,i)).*dat));
39     dp_exp(:,:,i) = abs(sim(:,:,i));
40 end
41
42 %% plot original data - hsv representation
43 figure(1); clf;
44 dathsv = zeros(size(dat,1),size(dat,2),3);
45 dathsv(:,:,1) = (angle(dat)+pi)./(2*pi);
46 dathsv(:,:,2) = ones(size(dat,1),size(dat,2));
47 dathsv(:,:,3) = abs(dat);
48 imshow(hsv2rgb(dathsv));
49 title('original object [hsv]');
50
51 %% initial guess for object
52 object = complex(rand(201),rand(201));
53
54 %% PIE loop
55 for i = 1:n
56
57     fprintf(['PIE iteration ' num2str(i,'%03d') ', error: ']);
58
59     %% loop over the 4 positions
60     for pos=1:4
61
62         obj = probe(:,:,pos).*object;
63         objnew = ifft2(dp_exp(:,:,pos).*exp(sqrt(-1).*angle(fft2(obj))));
64         update_function= conj(probe(:,:,pos)).*abs(probe(:,:,pos))./...
65             (conj(probe(:,:,pos)).*probe(:,:,pos)+alpha);

```

```

66     object_new = object +update_function.*(objnew-obj);
67
68     object = object_new;
69
70     err(:,:,pos) = (dp_exp(:,:,pos).^2 - (abs(fft2(obj))).^2).^2./(201.^2);
71     fprintf([' ' num2str(sum(sum(err(:,:,pos))), '%0.2d')]);
72
73     %% plot retrieved object in hsv representation
74     figure(2);
75     objecthsv = zeros(size(object,1),size(dat,2),3);
76     objecthsv(:,:,1) = (angle(object.*exp(sqrt(-1).*1*pi))+pi)./(2*pi);
77     objecthsv(:,:,2) = ones(size(object,1),size(object,2));
78     objecthsv(:,:,3) = abs(object)- (0.5+0.5*sign(abs(object)-1)).*...
79         (abs(object)-1);
80     imagesc(hsv2rgb(objecthsv)); drawnow;
81     title('retrieved object [hsv]');
82     end
83
84     %% calculate average error
85     avg_err(i) = sum(sum(mean(err,3)));
86     fprintf(['\n average error is: ' num2str(avg_err(i), '%0.2d') '\n'])
87 end
88
89 %% plot error
90 figure(3);
91 plot(log10(avg_err));
92 title('log10 of average reciprocal space error')
93 xlabel('PIE iterations')

```

# Erklärung

Die vorliegende Arbeit habe ich selbst verfasst und keine anderen als die angegebenen Quellen und Hilfsmittel benutzt.

Villigen PSI, den 22.10.2007

Martin Dierolf

# Acknowledgements

I want to thank all people that supported me during my studies and during this year of thesis work and helped me to accomplish this.

First I want to thank Prof. Dr. Othmar Marti for supervising this external thesis and so giving me the possibility to work on this exciting topic. I also want to thank Prof. Dr. Ute Kaiser, who has accepted the task to judge this manuscript.

I am deeply indebted to Prof. Dr. Franz Pfeiffer, who proposed this thesis and did a excellent job in supervising me here at PSI. I thank him for introducing me to the interesting field of synchrotron radiation research, for giving me the possibility to participate in many beamtimes during the last year, the large number of regular and spontaneous discussions, from which I highly profited, and for his advice in many other things.

I would like to thank Dr. Oliver Bunk for his constant support during the last year, many fruitful discussion, countless solved problems with computers or experimental equipment and several cups of tea.

I am grateful for a lot of helpful suggestions Dr. Andreas Menzel gave and for his support during measurements.

Dr. Ian Johnson gave me the first introduction to the PIE algorithm and many other useful advice.

Dr. Pierre Thibault came up with many new ideas how to improve our diffractive imaging experiments and reconstructions. Xavier Donath provided technical support and a very nice barbecue location.

I am very grateful for work Søren Kynde had already done on PIE, from

which I could highly profit. I would also like to mention Louise Sperling, who measured nice curved wavefront data.

I want to thank Dr. Christian David, Dr. Konstantins Jefimovs and Joan Vila for the good collaboration and in particular for their nano structures we could use for the x-ray experiments.

I profited a lot from collaborations, discussions and valuable assistance from many more people here at PSI. In particular, I would like to thank: Dr. Jörg Raabe, Dr. Marco Stampanoni, Edith Fuchsberger, Dr. Dilip Satapathy, Prof. Dr. Friso van der Veen, Charlotte Herr, Dr. Tilman Donath, Martin Bech, Dr. Chris Milne, Dr. Maik Kaiser, Renske van der Veen, Dr. Gerhard Ingold, and many more.

I thank Prof. Dr. Paul Walther for the opportunity to join his already overbooked electron microscopy course and Ulla Nolte for the preparation of the cytoskeletons.

I want to thank my friends ‘in Ulm und um Ulm und um Ulm herum’ for the many things we experienced together during the last years.

I gratefully acknowledge the financial and personal support I recieved from the ‘Evangelisches Studienwerk Villigst’ and in particular Dr. habil. Knut Berner and Prof. Dr. Eberhard Müller.

Ein ganz besonderer Dank gilt meinen Eltern, die mich all die Jahre in jeder erdenklichen Hinsicht unterstützt haben.